

## Article

# Trace Element Assemblages of Pseudomorphic Iron Oxyhydroxides of the Pobeda-1 Hydrothermal Field, 17°08.7' N, Mid-Atlantic Ridge: The Development of a Halmyrolysis Model from LA-ICP-MS Data

Valeriy V. Maslennikov <sup>1,\*</sup>, Georgy A. Cherkashov <sup>2,3</sup>, Anna V. Firstova <sup>2</sup>, Nuriya R. Ayupova <sup>1</sup>, Victor E. Beltenev <sup>2</sup>, Irina Yu. Melekestseva <sup>1</sup>, Dmitry A. Artemyev <sup>1</sup>, Aleksandr S. Tseluyko <sup>1</sup> and Ivan A. Blinov <sup>1</sup>

<sup>1</sup> Institute of Mineralogy, South Urals Federal Research Center of Mineralogy and Geoecology, Ural Branch, Russian Academy of Sciences, 456317 Miass, Russia

<sup>2</sup> Institute for Geology and Mineral Resources of the Ocean (VNIIOkeangeologia), Angliiskiy Av. 1, 190121 St. Petersburg, Russia

<sup>3</sup> Institute of Earth Sciences, St. Petersburg State University, 7/9 Universitetskaya Emb., 199034 St. Petersburg, Russia

\* Correspondence: mas@mineralogy.ru



**Citation:** Maslennikov, V.V.; Cherkashov, G.A.; Firstova, A.V.; Ayupova, N.R.; Beltenev, V.E.; Melekestseva, I.Y.; Artemyev, D.A.; Tseluyko, A.S.; Blinov, I.A. Trace Element Assemblages of Pseudomorphic Iron Oxyhydroxides of the Pobeda-1 Hydrothermal Field, 17°08.7' N, Mid-Atlantic Ridge: The Development of a Halmyrolysis Model from LA-ICP-MS Data. *Minerals* **2023**, *13*, 4. <https://doi.org/10.3390/min13010004>

Academic Editor:  
Mariko Nagashima

Received: 14 November 2022  
Revised: 16 December 2022  
Accepted: 17 December 2022  
Published: 20 December 2022



**Copyright:** © 2022 by the authors. Licensee MDPI, Basel, Switzerland. This article is an open access article distributed under the terms and conditions of the Creative Commons Attribution (CC BY) license (<https://creativecommons.org/licenses/by/4.0/>).

**Abstract:** Halmyrolysis, as one of the global processes of alteration of seafloor hydrothermal sediments, needs to be recognized in terms of mineral and trace element evolution to elaborate new criteria for metallogenic and geoecological forecasts with respect to ocean exploration. The purpose of this paper is to explain trace elements' behavior during the halmyrolysis of sulfide deposits. This task is resolved using an LA-ICP-MS analysis of iron oxyhydroxides (IOHs) on examples of oxidized pyrrhotite-rich diffusers of the ultramafic-hosted Pobeda-1 hydrothermal field (Mid-Atlantic Ridge). The IOHs formed after the sulfides were enriched in seawater-derived trace elements (Na, K, Mg, Ca, Sr, P, U, Mo, V, REE, Cr). Six trace element assemblages (TEAs) are statistically recognized for the IOHs. TEA-I (Cu, In, Sn, Bi, Se, Te) is inherited from chalcopyrite, isocubanite and bornite microinclusions. TEA-II is typical of Zn sulfides (Zn, Cd, Sb, Tl, Ag) interacted with seawater (Mg, U, Mo, Ni, Na, K) and hydrothermal fluid (Eu). TEA-III (Ca, Sr, Cu, Si, Se, P, As) reflects the inclusions of aragonite, opal, atacamite and possibly native selenium, while P and As occur as adsorbed oxyanion groups on IOHs or Ca-Fe hydroxyphosphates. TEA-IV (Al, Ga, Ge, Tl, W, Ti ± Mn, Co, Ba) indicates the presence of minor clays, Co-rich Mn oxyhydroxides and barite. TEA-V with Pb and V is closely related to TEA-VI with REEs except for Eu. The halmyrolysis of sulfides includes two stages: (i) oxidation of S(II) of primary sulfides and the formation of supergene sulfides, which scavenge the redox-sensitive elements (e.g., U, Mo, Ni, Eu), and (ii) oxidation of Fe (II) to Fe (III) and absorption of most elements of TEAs III, IV, V and VI by IOHs.

**Keywords:** iron oxyhydroxides; trace elements; halmyrolysis; Pobeda hydrothermal field; Mid-Atlantic Ridge

## 1. Introduction

Seafloor weathering (halmyrolysis) and the related dissolution, autocracking and reworking of consolidated seafloor massive sulfide (SMS) mounds have been suggested for the origin of sulfide breccias and fine-grained sulfide sandstones with zones of full oxidation, leaching and enrichment in modern SMS and ancient volcanic-hosted massive sulfide (VHMS) deposits [1–11]. A geochemical model of SMS formation can provide insights for evaluating the effect of oxidation on the economic values of sulfides and seafloor ecosystems [12–15].

Several recent publications proposed the geochemical models of hydrothermal partitioning of trace elements (TEs) in SMS systems [5,15–20]. The TEs are subdivided into

hydrothermal and seawater associations. A few publications are devoted to supergene and diagenetic TE partitioning in modern SMS [17,21] and ancient VHMS deposits [22].

Limited results are published on TE behavior in iron oxyhydroxides (IOHs), which are products of the seafloor weathering (halmyrolysis) of primary sulfides, the continuous oxidation of which would lead to metal mobilization [3,13,20,23–27]. Most studies consider the composition of the suspended IOHs in rising hydrothermal plumes of black smokers [28–31]. Only a few works examine the TEs in oxidation products of sulfide deposits [2,23,27,32–35].

The concentrations of Au, Cu, Sb, Co and Se in Au-rich gossans from the TAG hydrothermal field, Mid-Atlantic Ridge (MAR), are similar to those in secondary sulfides (digenite, covellite) indicating inheritance of this geochemical signature from primary sulfides [36]. The behavior of other trace metals (Zn, Pb, Sb, Cd, Tl, Hg, Se, Te, In, Ge, Ga, etc.) during the submarine oxidation of sulfides, however, becomes an important consideration for economic account and ecological forecast [27,34,37].

The most important achievement of the IOH study is the recognition of a negative Ce anomaly (influence of seawater) and a positive Eu anomaly (influence of hydrothermal fluid) [24,32,38]. It was found that Fe-gossans from the TAG hydrothermal field and ochres from the Skouriotissa VHMS deposit, Cyprus, display similar REE signatures that are likely retained from the primary sulfides [2]. Another significant phenomenon is the U enrichment of modern submarine gossans [23] and gossanites of ancient VHMS deposits [26]. The Se enrichment is documented in submarine gossanites and continental gossans of ancient VHMS deposits [39,40]. In general, the understanding of the phenomenon of TE partitioning during the seafloor oxidation of sulfides is still in progress [13,25,27,33,34,41–43].

Two types of oxidation are known: the direct oxidation of sulfides by oxygenated seawater and oxidation from Fe–Si-rich waning hydrothermal fluids [24,27,44]. In our paper, we focus on the in situ oxidation of pyrrhotite–pyrite–wurtzite diffusers. Special attention is paid to the morphological signatures of IOH types and their TE composition including REE contents. The purpose of our study is to recognize a range of TE assemblages (TEAs) of the IOHs. We try to clarify whether or not the TEs are leached, retained or absorbed from ambient seawater by oxidation products. Several TEAs are determined in the studied IOH to assess a proportion between the residual TEs from primary sulfides and seawater-derived TEs.

## 2. Geological Setting

The Pobeda massive sulfide hydrothermal fields (Pobeda-1, Pobeda-2 and Pobeda-3) were discovered in the 37th cruise (2014–2015) of R/V *Professor Logatchev* by the Polar Marine Geosurvey Expedition (PMGE) in collaboration with VNIIOkeangeologia, St. Petersburg, Russia [45,46]. These fields are located on the eastern flank of the MAR rift valley (17°08' N) (Figure 1) on a western slope of an oceanic core complex at a depth of 1950–3100 m. The host rocks are serpentinized peridotites, serpentinites, gabbro, basalts and dolerites [47].

The active Pobeda-1 hydrothermal field (17°08.7' N, 46°23.44' W) is located at a depth of 1950–2400 m. It consists of four sulfide bodies (mounds about 10 m in height) with sulfide chimneys and fragments of sulfide chimneys and diffusers, ferruginous gossany crusts and metalliferous sediments. The hydrothermal field is associated with basalts, peridotites and gabbro-norites [45,46,48,49].

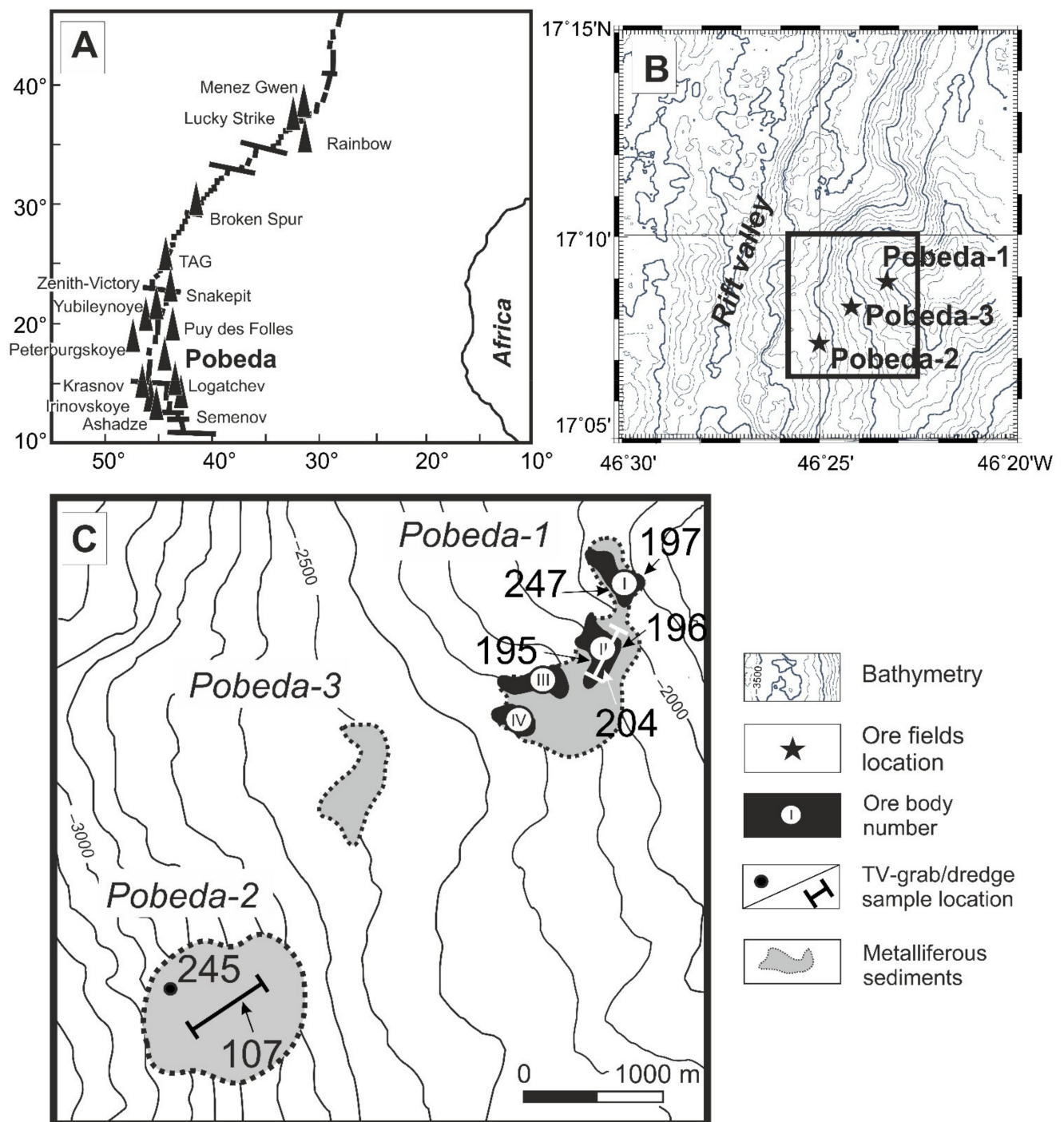


**Figure 1.** Geological setting of the Pobeda massive sulfide hydrothermal fields. (A) Location of the Pobeda cluster at the Mid-Atlantic Ridge; (B) Position of the Pobeda-1, 2 and 3 hydrothermal fields at the Mid-Atlantic Ridge bathymetry; (C) Detailed scheme of hydrothermal fields with location of sampling stations [45,46].

### 3. Materials and Methods

SMS samples were collected using a TV-grab and a dredge [45,46] from massive sulfide bodies I and II of the Pobeda-1 hydrothermal field (Figure 1). The morphogenetic types and mineral composition of the samples were previously described in [17,48–50].

All samples were studied using reflected light microscopy. The surfaces of some sulfides were etched by concentrated  $\text{HNO}_3$  mixed with a  $\text{CaF}_2$  powder. Microinclusions

of minerals in pyrite and IOHs were identified using a Vega 3sbu Tescan SEM equipped with an Oxford Instruments X-act EDS and a REMMA-2M SEM equipped with a Link EDS at the Institute of Mineralogy, South Urals Federal Research Center of Mineralogy and Geoecology UB RAS, Miass, Russia (IMin SU FRC MG UB RAS).

The contents of the TEs ( $^{23}\text{Na}$ ,  $^{25}\text{Mg}$ ,  $^{27}\text{Al}$ ,  $^{29}\text{Si}$ ,  $^{31}\text{P}$ ,  $^{39}\text{K}$ ,  $^{43}\text{Ca}$ ,  $^{49}\text{Ti}$ ,  $^{51}\text{V}$ ,  $^{52}\text{Cr}$ ,  $^{55}\text{Mn}$ ,  $^{59}\text{Co}$ ,  $^{60}\text{Ni}$ ,  $^{65}\text{Cu}$ ,  $^{66}\text{Zn}$ ,  $^{75}\text{As}$ ,  $^{77}\text{Se}$ ,  $^{95}\text{Mo}$ ,  $^{107}\text{Ag}$ ,  $^{111}\text{Cd}$ ,  $^{118}\text{Sn}$ ,  $^{121}\text{Sb}$ ,  $^{125}\text{Te}$ ,  $^{182}\text{W}$ ,  $^{197}\text{Au}$ ,  $^{205}\text{Tl}$ ,  $^{208}\text{Pb}$ ,  $^{209}\text{Bi}$ ,  $^{232}\text{Th}$ ,  $^{238}\text{U}$ ,  $^{139}\text{La}$ ,  $^{140}\text{Ce}$ ,  $^{141}\text{Pr}$ ,  $^{146}\text{Nd}$ ,  $^{147}\text{Sm}$ ,  $^{153}\text{Eu}$ ,  $^{157}\text{Gd}$ ,  $^{159}\text{Tb}$ ,  $^{163}\text{Dy}$ ,  $^{165}\text{Ho}$ ,  $^{166}\text{Er}$ ,  $^{169}\text{Tm}$ ,  $^{172}\text{Yb}$ ,  $^{175}\text{Lu}$ ) of sulfides and IOHs were analyzed on a New Wave 213-nm solid-state laser microprobe coupled to an Agilent 7700 $\times$  quadrupole ICP-MS housed at the IMin SU FRC MG UB RAS. The analyses were performed by ablating spots ranging in size from 40 to 80  $\mu\text{m}$ . The laser repetition rate was 10 Hz and the laser beam energy at the sample was maintained between 3 and 4  $\text{J}/\text{cm}^2$ . The analysis time for each spot was 90 s, comprising a 30 s measurement of the background and a 60 s measurement. The mass-spectrometer was calibrated by use of multi-elemental solutions. The TE contents were calculated in the Iolite program using international glass (NIST SRM-612, USGS GSD-1G) and sulfide (USGS MASS-1) standards and  $^{57}\text{Fe}$  as an internal standard for the quantification of pyrite (46.5%) and pyrrhotite (63.6%).

For the IOHs, the mass spectrometer was calibrated using calibration standard reference materials NIST SRM-610 and NIST SRM-612. The level of molecular oxides ( $^{232}\text{Th}^{16}\text{O}/^{232}\text{Th}$ ) was maintained below 0.3–0.4%. The  $^{238}\text{U}/^{232}\text{Th}$  ratio, when tuned to NIST SRM-610, was close to 1:1. All mass fractions of elements for international standard reference materials were taken from the GeoReM database. Data were processed and calculated in the Iolite software package [51]. USGS GSD-1g and NIST SRM-610 were used as external standards. For “pure” IOHs with a small amount of TEs, normalization used  $^{57}\text{Fe}$  62.8 wt% with an additional deduction of TEs. For heavily contaminated IOHs and their mixtures with a nonmetallic host matrix, the calculation was carried out in two stages. The concentrations of elements were first calculated based on the stoichiometric content of Fe in the mineral, then the measured contents of all main elements (Na, Mg, Al, Si, P, Ca, Mn, Fe, Cu, Zn) were recalculated into oxide forms and normalized to 100 wt% of the substance (in some cases, the amount decreased to 95–98 wt% due to undetectable  $\text{H}_2\text{O}$ ,  $(\text{OH})^-$ , O, S, C, etc.). After normalization, the measured values of  $\text{Fe}_2\text{O}_3$  were recalculated to the oxide-free form and new values of  $^{57}\text{Fe}$  were used as an internal standard in a new iteration of recalculation [52]. Detection limits (DL) of the TEs detected for the IOHs are much lower than the obtained values except for Au, Bi, Te (DL 0.01–0.10 ppm) and Se (DL 0.1–1.0 ppm). In rare case, if the value is below DL, we used a half DL value to complete the statistical calculation. Most REE contents of sulfides are below DL (0.10–0.01 ppm).

Note that the scanning capability of LA-ICP-MS cannot be used to distinguish between homogeneously distributed nano-inclusions, absorbed or lattice bound elements in sulfides [18,53–55]. This problem remains pertinent for the IOH aggregates, as well.

In this paper, the LA-ICP-MS data were processed in the Statistica program v.10 using correlation, cluster and factor (Q-mode and R-mode) analyses to recognize the TEAs. First, they were calculated following the maximal correlation way method (MCW) [56]. In the MCW analysis, the source material is half of the square correlation matrix, in which only statistically significant correlation coefficients are recorded. The maximum module of the correlation coefficients is ranged for each of the following elements. A new selection is not made, if the element with the maximum correlation coefficient has already been selected. Several associations with high correlation coefficients are divided by minimum values of correlation coefficients.

Factor analysis was used to analyze the interrelationships among large number of variables and to explain these variables. We compared the results of Q-mode and R-mode factor analyses. The difference between Q-mode and the R-mode is that the latter searches for cluster variables on a set of cases, while the Q-mode clusters the cases rather than the variables establishing the functional composition of a group on a set of issues [57]. R-mode factor analysis is performed using a correlation matrix for all IOH types: it examines the

relationships between the measures of the variables to understand how they are grouped together and related to each other. The correlation coefficients were revised using diagrams.

The following symbols are used for minerals in the figures: Bn, bornite; Ccp, chalcopyrite; Gee, geerite; ISS, Cu-Fe-S intermediate solid solution; CuS\*—digenite + geerite + covellite; Pyh, pyrrhotite; Py, pyrite; *e*—euhedral; *s*—subhedral; *p*—pseudomorph after pyrrhotite; Sp, sphalerite; Wur, wurtzite; IOH, iron oxyhydroxides; Ata, atacamite; Op, opal; Arg, aragonite.

## 4. Results

### 4.1. Mineral Formation Sequences

Most of the studied samples of the Pobeda-1 hydrothermal field represent porous friable aggregates of sulfide diffusers, which are made up of pyrite, marcasite and pyrrhotite (Figure 2a) with a minor amount of wurtzite–sphalerite and rare isocubanite–chalcopyrite aggregates. Talc, opal, gallite  $\text{CuGaS}_2$ , atacamite, bornite, covellite, gypsum and aragonite are subordinate minerals. Accessory minerals are native gold, cobaltite, argentite, and a U oxide [49,50,58,59]. Rare cobaltite grains are related to isocubanite aggregates. Native gold ( $<1 \mu\text{m}$  in size) occurs in cobaltite, IOHs and pyrite–chalcopyrite and pyrite–sphalerite intergrowths. The U mineralization occurs in the cracks and intergranular space of pyrite [35]. Greigite was found as a primary mineral in pyrite-rich samples, while geerite was detected in the assemblage with chalcopyrite, digenite and bornite [17]. In bottom sediments, rare Zn minerals (zinc phosphates, zincite, willemite, gahnite and Zn-forsterite) are described for the first time in the MAR [49,60]. In addition to IOHs, metalliferous sediments contain trace quantities of atacamite, calcite, muscovite, kaolinite, quartz, barite, pyroxenes, serpentine, talc, olivine, epidote, magnetite, ilmenite and sulfides [35].

In the studied fragment of a sulfide diffuser, the pyrrhotite crystals are replaced by pyrite and IOHs (Figure 2). Relics of pyrrhotite are retained in a fine-grained pyrite or wurtzite coating, which incrust the walls of the conduits (Figure 2b,c). In the polished section, the maximum angle between the pinacoid {0001} and rhombohedron is about  $62^\circ$ , which is typical of pyrrhotite crystals ( $62^\circ 18'$ ). Incomplete cleavage of pyrite pseudomorphs is characteristic of the pyrrhotite crystals (parallel to pinacoid {0001} and rhombohedron direction), while anhydrite shows complete square-shaped cleavage (about  $90^\circ$ ) [61]. The fragments of platy pyrrhotite crystals are replaced and overgrown by a lacy network of pyrite and marcasite. The net venation contour rim and porous areas are typical of pyrite pseudomorphs after pyrrhotite crystals. Some pseudomorphous pyrite is replaced by secondary chalcopyrite and later digenite and geerite (Figure 2c) [17]. Boxy fine-grained pyrite pseudomorphs after pyrrhotite crystals comprise the porous pyrite aggregates (Figure 2d). Boxy shapes form due to a decreasing volume of pyrite in comparison with pyrrhotite due to the differences in the volume of unit-cell in these minerals; this occurs by at least 8% [61].

Several morphological IOH types were identified in the samples. Typical relict cleavage is recognized in the fine-grained porous dark gray IOH-1 pseudomorphs after pyrrhotite crystals (Figure 2e). These immature IOHs, which are recrystallize to light gray crystalline goethite, partly replace pyrrhotite crystals (IOH-2), as well as massive pyrite–pyrrhotite aggregates (IOH-3) (Figure 2f,g). IOH-2 is overgrown by interstitial microporous IOH-4 aggregates. It is suggested that IOH-4 formed after Fe-rich wurtzite (Figure 2h). Some cavities in the IOH aggregates are filled with clastic IOH-5 (Figure 2i). The presence of rare relict pyrite, wurtzite, chalcopyrite, bornite and sphalerite inclusions and intergrows with atacamite is typical of all IOH types.

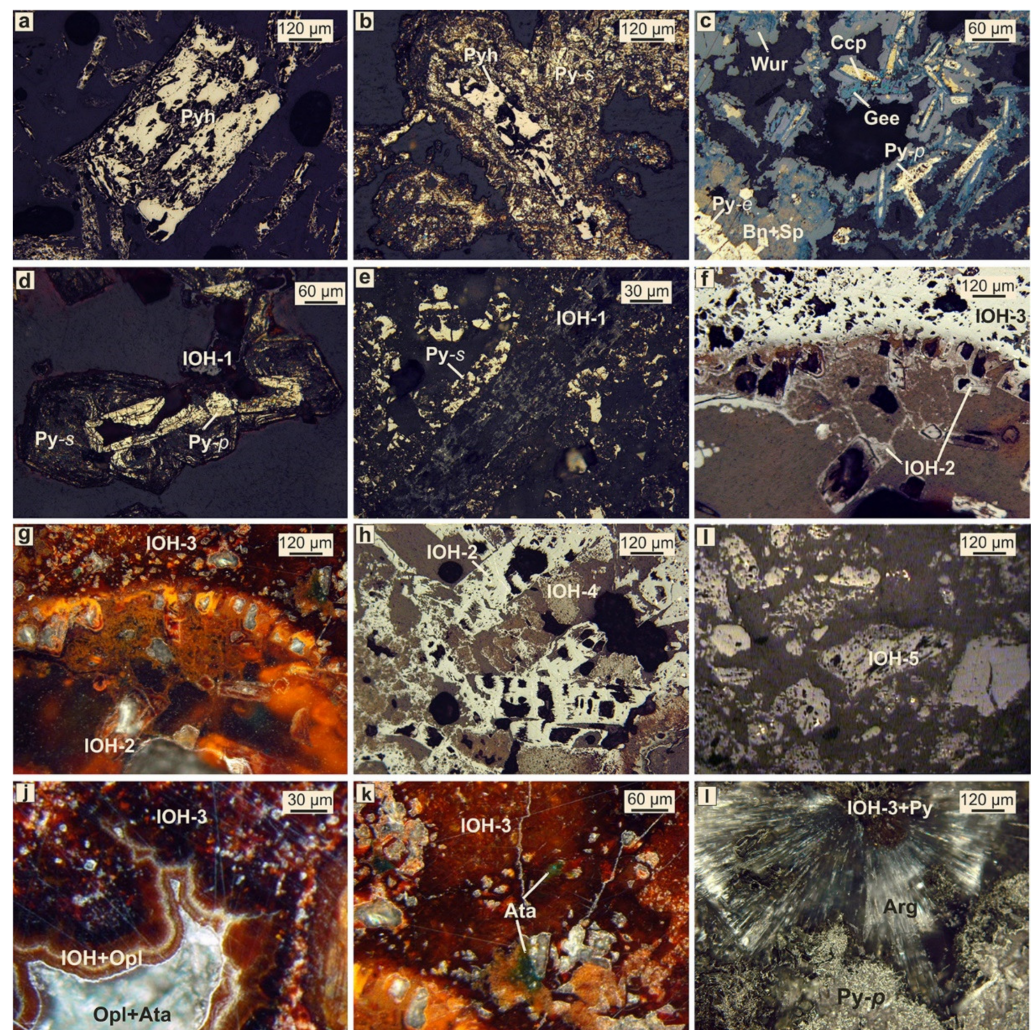


**Figure 2.** Morphology of pyrrhotite (Pyh), pyrite (Py) and IOHs of the Pobeda-1 hydrothermal field: (a) Euhedral pyrrhotite crystal; (b) Relict pyrrhotite crystal replaced by secondary pyrite (Py-s); (c) Pseudomorphic pyrite (Py-p) and chalcopyrite (Ccp) after subhedral pyrrhotite crystals overgrown by wurtzite (Wur) with bornite–sphalerite–geerite (Bn+Sp, Gee) assemblage; (d) Pseudomorphic boxy pyrite after pyrrhotite crystals (Py-p) replaced by IOHs; (e) Immature poorly crystalline pseudomorphic IOH-1 after pyrrhotite crystal; (f) Crystalline pseudomorphs after subhedral pyrrhotite (IOH-2) and after massive pyrite–pyrrhotite aggregates (IOH-3) in the wall of the conduit; (g) The same in dark field view; (h) Interstitial dark porous IOH-4 aggregates between IOH-2 pseudomorphs after subhedral pyrrhotite crystals; (i) Clastic IOH-5 with relict pyrite inclusions; (j) Opal (Op+Ata) in IOH-3; (k) Atacamite (Ata) in IOH-3; (l) Aragonite (Arg) in assemblage with pyrite and minor IOHs. Reflected light (a–f,h,i); dark field images (g,j–l).

Thus, pyrrhotite is mainly replaced by pyrite and IOH aggregates. The wurtzite–chalcopyrite and isocubanite aggregates are transformed into bornite–digenite–geerite assemblages commonly mixed with secondary sphalerite. The end-members of this mineral formation sequence are diverse IOHs including goethite, which are characterized by different morphology and fabric.

It is suggested that the mineral sequences in the studied samples are a result of hydrothermal growth and halmyrolysis. The isocubanite–wurtzite–pyrrhotite–pyrite assemblage together with cobaltite, native gold and gallite is related to a high- or moderate-temperature hydrothermal process. During the early halmyrolysis, pyrrhotite is replaced by pyrite, while isocubanite and wurtzite are replaced by sphalerite, bornite, digenite, geerite and covellite in assemblage with pyrite and barite. During late halmyrolysis, the Cu

sulfides are transformed to atacamite, while pyrite is replaced by IOHs in assemblage with opal and rare uraninite. In the apron of the hydrothermal field, the IOHs-rich metalliferous sediments are mixed with carbonates and aluminosilicates, ilmenite and magnetite derived from host peridotite, which were previously studied [34] and are not a subject of our paper.

#### 4.2. TEs in Sulfides and IOHs

The contents of TEs, except for the REEs, are presented herein for the hydrothermal and supergene sulfides and IOH types of the Pobeda-1 hydrothermal field. The median contents are shown in Table 1 and the full data are shown in Table S1.

**Table 1.** Median TE contents of sulfides and IOH types of the Pobeda-1 hydrothermal field, ppm.

Mineral	ISS	Sp + Bn	CuS *	Wur	Py-e	Py-s	Pyh	Py-p	IOH-1	IOH-2	IOH-3	IOH-4	IOH-5
n	23	10	11	28	20	15	32	36	31	46	37	16	11
V	0.13	3.6	3.1	0.2	1.31	9.0	1.03	4.9	65	104	191	228	222
Mn	9.0	27	23	70	1.01	1.2	41.9	1775	190	188	174	283	111
Fe,%	38.6	30.5	4.4	11	45.45	45.6	63.0	46.1	55.1	56.7	55.7	54.9	58.2
Co	1730	1793	2170	334	3035	1107	0.23	3.5	11	1.5	1.4	2.9	2.8
Ni	22	140	310	0.8	157	64	6.9	24.5	58	3.3	2.9	4.1	10
Cu,%	25.5	16.8	60.5	0.5	0.58	0.6	0.08	0.15	0.90	0.25	3.19	3.71	2.45
Zn,%	0.5	19.5	3.8	54	0.01	0.05	0.03	0.02	0.37	0.21	0.18	0.17	0.10
Ga	2.0	28	35	36	0.126	0.3	DL	0.2	1.5	1.2	1.5	2.6	2.3
Ge	DL	11	7.8	35	0.88	1.0	3.1	3.3	11	12	12	10	2.6
As	0.74	155	144	55	31	162	5	13.7	235	406	471	443	186
Se	221	99	116	6.0	106	53	DL	3.1	45	239	157	112	11
Mo	DL	88	246	0.4	13.5	48	3.1	71.3	892	692	644	642	196
Ag	16.01	81	135	16	7.4	9.0	4.43	4.2	2.0	0.4	0.2	0.3	0.3
Cd	19.6	120	23	782	1.4	0.6	DL	0.12	0.40	0.06	0.06	0.04	0.02
In	4.8	6.4	3.3	0.05	0.3	0.05	DL	0.01	0.02	0.10	0.09	0.09	0.17
Sn	2.46	10.9	12	11	0.5	0.4	2.88	2.20	5.3	4.8	6.9	26.9	7.5
Sb	DL	34	55	159	0.8	5.9	DL	1.87	20	11	13	13	10
Te	10.4	2.2	1.3	0.05	1.5	0.8	DL	0.33	0.5	3.2	2.5	1.5	0.5
Ba	DL	1.0	0.2	0.01	DL	0.2	DL	0.71	5.8	4.4	4.0	3.9	1.3
W	DL	0.2	0.4	0.02	DL	0.0	DL	0.06	1.0	0.45	0.60	0.79	0.58
Au	0.10	0.5	0.8	0.09	0.3	0.2	DL	0.21	0.2	1.4	1.3	3.5	0.8
Tl	DL	5.6	12	0.02	1.1	1.3	0.29	4.30	1.0	0.28	0.28	0.40	0.15
Pb	1.14	253	235	141	21.2	23	42.7	33.9	85	126	144	123	78
Bi	0.14	0.4	0.15	0.002	3.9	0.8	DL	0.10	0.07	0.36	0.60	0.95	0.47
U	DL	13	45	0.02	0.85	4.6	DL	8.90	100	61	54	53	29
Na	35.7	640	3050	12	40	115	40	349	6540	5490	6440	7995	6510
Mg	DL	162	767	2,3	24,6	54	31,55	408	4520	2019	1516	2590	1916
Al	DL	68	6.8	0.44	3.5	18	5.1	17.4	60	51	110	179	325
Si,%	0.16	0.069	0.05	0.08	0.05	0.03	0.04	0.14	0.85	1.83	1.73	1.88	1.92
P	230	179	93	155	65.5	73	430	189	2390	3040	3050	3610	2150
K	11.5	89	307	3	6.1	24	12	43	560	411	446	440	316
Ca	130	73	100	DL	145	DL	240	60	320	1025	1360	1815	168
Sr	DL	0.8	1.8	DL	0.10	0.26	DL	0.66	11	49	48	59	5.9
Cr	DL	1.8	DL	DL	DL	DL	DL	11.6	15	8.0	6.9	6.5	49
Ti	9.0	12.8	6.6	7.5	11.4	8.4	DL	DL	4.8	0.9	1.2	1.8	9.3

ISS—Cu-Fe-S intermediate solid solution; Sp + Bn—fine-grained intergrowth of supergene bornite and sphalerite; CuS \*—digenite + geerite + covellite; Sp—sphalerite; Pyh—pyrrhotite; Pyrite: Py-e—euhedral; Py-s—subhedral; Py-p—pseudomorphous after pyrrhotite; IOH types: IOH-1—immature pseudomorphous after subhedral pyrrhotite; IOH-2—crystalline pseudomorphous after subhedral pyrrhotite; IOH-3—pseudomorphous after massive pyrite-pyrrhotite aggregates; IOH-4—interstitial; IOH-5—clastic; n—number of LA-ICP-MS analyses; DL—below detection limit.

The isocubanite–chalcopyrite aggregates are characterized by significant contents of Co, Se and Te. The higher contents of Co, Ni, Pb, Ag, Sb, Tl, As, Mo, U, Mg, K and Na are typical of pseudomorphous Cu sulfides after isocubanite–chalcopyrite aggregates. The high Se contents (av. 121 ppm) of digenite are inherited from the isocubanite–chalcopyrite

aggregates (Table S1). The Fe-rich and Cd-poor wurtzite has higher Ga and Ge contents and slightly elevated Se, Co, Sb and Ag contents. In addition, the Mo, U, Co and U contents increase in supergene fine-grained sphalerite–bornite intergrowths formed after wurtzite and isocubanite–chalcopyrite aggregates. The high-temperature hydrothermal subhedral and euhedral pyrite associated with ISS displays high Co and moderate Ni, As and Se contents [17]. Pyrrhotite is characterized by the lower contents of almost all elements. The Mn, Mo, U, Mg and Na contents in pseudomorphic pyrite after pyrrhotite are higher than in pyrrhotite.

The IOHs differ from sulfides in higher contents of V, Mn, As, Se, Mo, U, Ba, Na, Mg, Al, Si, P, Ca, K, Sr and Cr (Table 1). The TE composition of IOH types is similar to each other. The interstitial IOH-1 has slightly higher contents of Ni, Mo, U, Ba, Mg, K and Ti, whereas the clastic IOH-5 has slightly higher contents of Cr, Si and Al.

Thus, supergene sulfides have the elevated contents of Na, K, Mg, Ni, U, Mo, V, W and Al in comparison with hydrothermal sulfides. All IOH types have the highest contents of these elements, as well as Au, Sr, Si, Ca, As, P and Cr in comparison both with hydrothermal and supergene sulfides. The contents of some elements (Co, Ni, Zn, Cd, Ag) decrease in a sulfide–IOH range. The contents of selected elements (Se, Te, Bi) remain similar in IOHs and sulfides.

#### 4.3. Rare Earth Elements of IOHs

In sulfides of the Pobeda-1 hydrothermal field, the REE contents are below the detection limits of the LA-ICP-MS analysis in contrast to all IOH types (Table 2). The REE contents of IOHs vary in a range of one–two orders of magnitude (Table S2). The IOH types exhibit almost similar REE patterns suggesting they all formed in similar chemical environments in spite of their different morphology. The exception is clastic IOH-5 enriched in light and heavy REEs (LREE and HREE, respectively). IOH-1 displays the highest Eu contents. The contents of some REEs increase in a range from IOH-1 to IOH-5, except for Eu, which is concentrated in immature IOH-1.

**Table 2.** Median REE contents of IOH types of the Pobeda-1 hydrothermal field, ppm.

	IOH-1	IOH-2	IOH-3	IOH-4	IOH-5		IOH-1	IOH-2	IOH-3	IOH-4	IOH-5
La	0.39	0.34	0.52	0.56	0.56	Tb	0.01	0.005	0.013	0.01	0.03
Ce	0.41	0.29	0.30	0.48	0.55	Dy	0.08	0.04	0.11	0.15	0.18
Pr	0.10	0.07	0.09	0.12	0.17	Ho	0.02	0.009	0.02	0.02	0.04
Nd	0.55	0.31	0.46	0.56	0.80	Er	0.04	0.02	0.09	0.10	0.17
Sm	0.04	0.02	0.04	0.04	0.12	Tm	0.005	0.001	0.007	0.004	0.01
Eu	0.64	0.25	0.25	0.25	0.29	Yb	0.02	0.013	0.07	0.11	0.12
Gd	0.07	0.04	0.11	0.09	0.12	Lu	0.004	0.003	0.006	0.014	0.013

The IOHs show a negligible negative Ce anomaly and a pronounced Eu anomaly (Table 3). The Eu anomaly in immature IOH-1 is larger than that in other IOHs especially in IOH-5. In all IOH types, the negative Ce anomalies are similar (0.3–0.4) and are slightly variable (0.1–0.7). The  $LREE^{NASC}/HREE^{NASC}$  ratios are highly variable (0.2–3.7), while their average values are similar except for the clastic IOH-5, which is enriched in HREEs.

**Table 3.** REE data for IOH types of the Pobeda-1 hydrothermal field.

IOH-1	Ce <sub>an</sub>	Eu <sub>an</sub>	LREE <sup>NASC</sup> /HREE <sup>NASC</sup>	La <sup>NASC</sup> /Yb <sup>NASC</sup>	IOH-4	Ce <sub>an</sub>	Eu <sub>an</sub>	LREE <sup>NASC</sup> /HREE <sup>NASC</sup>	La <sup>NASC</sup> /Yb <sup>NASC</sup>
av	0.4	75	0.7	1.1	av	0.3	18	0.4	1.2
dv	0.1	104	0.5	0.9	dv	0.1	14	0.3	2.6
max	0.7	593	2.3	2.8	max	0.5	56	1.1	10.6
min	0.1	15	0.2	0.1	min	0.1	6	0.2	0.1
med	0.4	44	0.5	0.6	med	0.3	13	0.3	0.4
IOH-2	Ce <sub>an</sub>	Eu <sub>an</sub>	LREE <sup>NASC</sup> /HREE <sup>NASC</sup>	La <sup>NASC</sup> /Yb <sup>NASC</sup>	IOH-5	Ce <sub>an</sub>	Eu <sub>an</sub>	LREE <sup>NASC</sup> /HREE <sup>NASC</sup>	La <sup>NASC</sup> /Yb <sup>NASC</sup>
av	0.4	45	0.8	2.9	av	0.4	19	0.3	0.3
dv	0.1	46	0.6	3.6	dv	0.1	28	0.2	0.2
max	0.6	230	3.7	15.1	max	0.7	102	0.6	0.7
min	0.1	9	0.2	0.2	min	0.1	6	0.2	0.1
med	0.4	29	0.6	1.4	med	0.4	9	0.3	0.2
IOH-3	Ce <sub>an</sub>	Eu <sub>an</sub>	LREE <sup>NASC</sup> /HREE <sup>NASC</sup>	La <sup>NASC</sup> /Yb <sup>NASC</sup>	Ce anomaly: $Ce_{an} = Ce/Ce^{NASC} / (0.5 \times La/La^{NASC} + 0.5 \times Nd/Nd^{NASC})$ Eu anomaly: $Eu_{an} = Eu/Eu^{NASC} / (0.5 \times Sm/Sm^{NASC} + 0.5 \times Cd/Cd^{NASC})$				
av.	0.3	30	0.6	1.0					
dv.	0.2	40	0.6	1.6					
max.	1.1	208	3.8	6.8					
min.	0.1	3	0.1	0.1					
med.	0.3	16	0.3	0.4					

The REE data are normalized to the average REE concentrations of the North American Shale Composition (NASC) shale [62]. Values: av., average; dv, standard deviation; max, maximum; min, minimum; med, median.

#### 4.4. Correlation Analysis

Correlation coefficients (Table 4 and Table S3) calculated by the Pearson method reveal various TEAs. Despite the different valences and positions in their range, the highest positive correlation coefficients of the IOHs are typical of the REEs. The REEs have a high positive correlation with P, As, V, Pb and Al. Calcium and Sr have a strong positive correlation (0.94); both elements have weaker correlations with P, As, V and Pb (which have also correlations with REEs) and furthermore, Ca and Sr are also enclosed in other TEAs with Cu, Si, Se, Sn and Bi. Zinc, Sb, Ag, Tl, Cd and Ga are the elements related to isomorphic substitution in sphalerite and wurtzite, while Mg, U, Mo, W and Ni are seawater-derived elements typical of supergene sulfides intergrown with sphalerite-2. The correlation between Bi, Te, Au, Sn, In, Cu and Se is characteristic of the chalcopyrite–ISS microinclusions.

#### 4.5. MCW Analysis

Each IOH type of the Pobeda-1 hydrothermal field exhibit different MCW-calculated TEAs (Table S4). The MCW calculation for all IOH-1–5 types yields 13 TEAs with a positive correlation: I(Nd + Pr + Sm) + Tb + II(Er + Ho + Dy + Yb + Tm + Lu + Gd) + III(Ce + La + Pb) + IV(Ge + As + P) + V(V + Al + Ga + W + Eu) + VI(Sb + Zn) + VII(Ni + Mg) + VIII(U + Mo) + IX(Cd + Ag + Tl) + X(K + Ba + Mn + Co + Au) + XI(Bi + Te) + XII(Se + Si + Sr + Ca + Cu) + XIII(Sn + In + Ti) – Na.

The group of REEs, except for Eu, is subdivided into three TEAs: TEAs-I and III include LREEs, while TEA-II contains HREEs. In TEAs-III, Pb has a strong positive correlation with La and Ce. TEA-IV indicates substitution between P and As. In TEAs-V, Eu demonstrates an independent position from other REEs and correlates with clay or seawater-derived elements. TEAs-VI–X include elements commonly substituted in structure of Zn sulfides (Cd, Ag, Tl, Sb) and derived from seawater (Mg, Ni, U, Mo). TEA-X includes elements probably concentrated in Mn oxyhydroxides. TEA-XI most likely reflects the presence of relict tellurobismuthite. TEA-XII may represent an opal–aragonite–atacamite assemblage with native selenium. Relict Cu sulfides are registered by the correlation of Sn and In, as well as by the correlation of Bi, Te and Se. These TEs are probably inherited from relict microinclusions of chalcopyrite and isocubanite replaced by bornite, digenite, geerite, covellite and atacamite.

**Table 4.** The correlation coefficients of TEs calculated for all IOH types of the Pobeda-1 hydrothermal field.

P	As	Ge	Pb	V	Si	Sr	La	Ca	W	Sb	Lu	Cd	Ni	U	Ag	Zn	Mg	Sb
	0.87	0.68	0.58	0.57	0.56	0.55	0.53	0.49	0.42	0.41	0.40		0.57	0.43	0.43	0.43	0.40	0.39
V	Lu	W	Al	La	Ga	P	Eu	Ce	As	Pb	In	U	Zn	Mo	Sb	Ni	Mg	Tl
	0.72	0.69	0.69	0.68	0.63	0.57	0.56	0.53	0.49	0.48	0.46		0.64	0.62	0.61	0.59	0.55	0.29
La	Ce	Lu	Pb	V	Eu	P	As	Ge	Sr	Al	Ca	Cu	Ca	Sr	Si	Se	Sn	Bi
	0.86	0.82	0.73	0.68	0.54	0.53	0.53	0.50	0.49	0.42	0.42		0.66	0.63	0.61	0.46	0.33	0.29
Eu	W	Ce	Sb	Lu	Zn	Ga	Pb	V	La	Al	Ni	In	Sn	Al	Ga	V	Bi	Si
	0.72	0.64	0.63	0.60	0.59	0.57	0.56	0.56	0.54	0.52	0.44		0.80	0.55	0.49	0.46	0.37	0.37
Lu	La	Ce	V	Pb	Eu	Al	Co	W	P	Ga	Sr	Se	Si	Cu	Sr	Ca	Ge	Te
	0.82	0.77	0.72	0.64	0.60	0.56	0.43	0.43	0.40	0.40	0.37		0.62	0.46	0.41	0.36	0.31	0.28
Sb	Zn	Ni	Eu	Mg	W	U	Mo	P	Tl	Cd	Ge	Mo	U	Sb	Zn	Ni	Mg	Cd
	0.72	0.64	0.63	0.62	0.61	0.61	0.53	0.41	0.40	0.39	0.38		0.62	0.53	0.50	0.35	0.34	0.27
Sr	Ca	Si	Cu	P	Pb	Ge	La	As	Mn	Se	V	Co	Mn	Lu	La	V	Au	Ge
	0.94	0.81	0.63	0.55	0.52	0.52	0.49	0.47	0.47	0.41	0.39		0.50	0.43	0.41	0.39	0.39	0.38
Pb	La	Ge	Lu	As	Ce	P	Eu	Sr	V	Ca	Si	Ba	Ge	P	As	Mn		
	0.73	0.71	0.64	0.62	0.58	0.58	0.56	0.52	0.48	0.39	0.35		0.42	0.38	0.36	0.33		
W	Ga	Eu	V	Al	Sb	Zn	Lu	P	Ce	Mg	Tl	Bi	Te	Au	Sn	In	Ga	
	0.73	0.72	0.69	0.62	0.61	0.59	0.43	0.42	0.40	0.32	0.30		0.62	0.43	0.37	0.37	0.33	
Al	Ga	Cr	V	W	Ce	Lu	In	Eu	La	Sn		Mn	Co	Sr	Ca	Ge	Ba	P
	0.69	0.70	0.69	0.62	0.58	0.56	0.55	0.52	0.42	0.31			0.50	0.47	0.37	0.35	0.33	0.32
As	P	Ge	Pb	La	Si	V	Sr	Ca	Ba	Lu	Co	Ag	Cd	Tl	Na	Ni	Zn	U
	0.87	0.74	0.62	0.53	0.51	0.49	0.47	0.38	0.36	0.34	0.32		0.43	0.37	0.35	0.30	0.27	0.25
Si	Sr	Ca	Se	Cu	P	Ge	As	In	Pb	La	Sn	Na	Mg	Ag	Ni	Sb	Co	Ti
	0.81	0.76	0.62	0.61	0.56	0.53	0.51	0.37	0.35	0.34	0.31		0.43	0.35	0.3	0.21	0.2	0.2
Ce	La	Lu	Eu	Pb	Al	V	W	Ti	In	Ga	P	Te	Bi	Pb				
	0.86	0.77	0.64	0.58	0.58	0.53	0.40	0.40	0.38	0.35	0.34		0.62	0.31				
Ge	As	Pb	P	Si	Sr	La	Ba	Co	Sb	V	Eu	Au	Bi					
	0.74	0.71	0.68	0.53	0.52	0.50	0.42	0.38	0.38	0.37	0.34		0.43					
Mg	Ni	Zn	Sb	U	Na	Cd	Tl	Eu	Mo	W		Sn	In	Bi	Ca	Sr	Si	Al
	0.81	0.64	0.62	0.55	0.43	0.40	0.37	0.35	0.34	0.32			0.80	0.37	0.34	0.31	0.31	0.31
Ni	Mg	Zn	Sb	U	Cd	Tl	Eu	Mo	Na	K	W	Tl	Zn	Ni	Sb	Na	Ag	Cd
	0.81	0.67	0.64	0.59	0.57	0.48	0.44	0.35	0.30	0.29	0.29		0.49	0.48	0.40	0.37	0.37	0.36
Zn	Sb	Ni	U	Mg	W	Eu	Mo	Tl	Cd	Ga		Ti	Al	Sn	In	Ce		
	0.72	0.67	0.64	0.64	0.59	0.59	0.50	0.49	0.43	0.39			0.61	0.49	0.43	0.40		
Ca	Sr	Si	Cu	P	La	As	Pb	V	Mn	Se	Ge	Cr	Al	W	V	Eu		
	0.94	0.76	0.66	0.49	0.42	0.38	0.39	0.38	0.36	0.36	0.35		0.70	0.50	0.46	0.44		
Ga	W	Al	V	Eu	In	Lu	Zn	Sb	Ce	La			Critical coefficient is 0.29. $p < 0.001$					
	0.73	0.69	0.63	0.57	0.49	0.40	0.39	0.37	0.35	0.29			Number of analyses is 144 (Table S2)					

#### 4.6. Cluster Analysis

The cluster analysis revealed six clusters (A–F) of the elements or TEAs (Figure 3). TEA-A is probably related to a Mn crust. TEA-B combines an opal–aragonite mineral assemblage with phosphates and arsenates. TEA-C is related to Cu sulfides, while TEA-D contains elements typical of Zn sulfides (Cd, Ag, Tl, Sb) interacted with seawater (Mg, U, Mo, Ni). TEA-E shows a strong linkage of the REEs with Pb and V. TEA-F could reflect the presence of elements in trivalent form absorbed on the IOHs from clays or seawater.

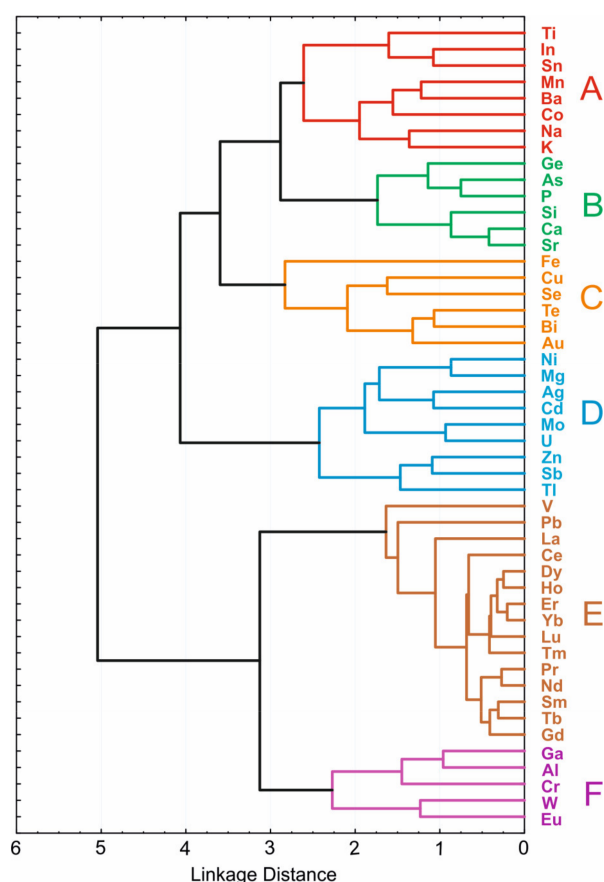


**Figure 3.** Tree diagram for 49 elements generated by cluster analysis. Complete linkage. Euclidian distance. All IOHs, Pobeda-1 hydrothermal field. TEAs related to: A—a Mn crust; B—an opal–aragonite mineral assemblage with phosphates and arsenates; C—Cu sulfides; D—Zn sulfides interacted with seawater; E—strong linkage of the REEs with Pb and V; F—elements in trivalent form absorbed on the IOHs from clays or seawater.

#### 4.7. Factor Analysis

In the Q-mode factor analysis, we artificially selected two groups of elements: (1) hydrothermal elements (Fe, Cu, Zn, Co, Se, Pb, Cd, Ag, In, Sn, Sb, Te, Au, Bi, Eu) and (2) those probably derived from seawater or clays or that have a dual nature (Mg, K, Na, Ni, U, Mo, W, Al, Ga, Ge, Ca, Sr, Si, As, P, REEs). We took into account the correlation matrix (Table S4) and selected the ranges of loadings on each factor using Q-mode factor scores with  $r > 0.3$  (Table 5).

Five factors responsible for the compositional variability of the IOHs of the Pobeda-1 hydrothermal field are recognized on the basis of Q-mode factor analysis (Table S4). Factor 1, which explains 24.5% of the variability, comprises positive and negative scores. The positive scores represent TEAs with (1) hydrothermal Zn, Cd, Sb, Tl and Ag typical of Zn sulfides, and (2) seawater-derived U, W and Mo, as well as Eu, which can have a dual nature. The negative scores are characteristic both of hydrothermal (isocubanite, chalcopyrite) and/or supergene (bornite, digenite, geerite, covellite) Cu sulfides.

Factor 2 explains 16.4% of the variability and can be related to the IOHs, which absorb REEs together with P, V and As oxyanions. Some elements can occur in the structure of goethite (Al, Ga, Co, W, Ti) and opal (Si, Ge) in assemblage with Zn-rich atacamite (Cu, Zn) and aragonite (Ca, Sr). This TEA characterizes the complete oxidation of sulfides. Relict Cu sulfides (Cu, Bi, Sn, In) can also remain in this assemblage.

**Table 5.** Q-mode factor scores for the IOH types of the Pobeda-1 hydrothermal field.

Factor 1	Ni	Zn	Eu	Sb	Cd	Mg	U	Ag	Tl	W	Mo	In
	0.790	0.722	0.678	0.653	0.615	0.610	0.555	0.488	0.486	0.432	0.355	−0.324
	Sn	Fe	Te	Au	Se	Cu	Bi					
	−0.346	−0.388	−0.413	−0.438	−0.481	−0.497	−0.564					
Factor 2	Fe	Ti	Gd	Nd	Tb	Zn	Cu	Pr	Mn	Pb	Dy	Tm
	0.363	−0.328	−0.330	−0.331	−0.335	−0.348	−0.363	−0.374	−0.374	−0.398	−0.420	−0.422
	Eu	Yb	Bi	Ge	Ho	As	Er	Co	Ce	Lu	Al	Sb
	−0.424	−0.430	−0.431	−0.432	−0.439	−0.443	−0.448	−0.460	−0.463	−0.463	−0.465	−0.484
	W	Ca	La	Si	Sr	Ga	V	P	Sn	In		
	−0.492	−0.517	−0.518	−0.519	−0.524	−0.532	−0.594	−0.636	−0.654	−0.730		
Factor 3	Ag	Cd	V	La	Ce	Eu	Tm	Tb	Er	Lu	Ho	Dy
	0.576	0.453	−0.371	−0.453	−0.470	−0.473	−0.478	−0.498	−0.501	−0.505	−0.507	−0.508
	Yb	Pr	Sm	Nd	Gd	Fe	Pb					
	−0.515	−0.543	−0.552	−0.552	−0.603	−0.621	−0.653					
Factor 4	Cu	Sr	Ca	Si	Bi	Au	Te					
	0.513	0.423	0.380	0.341	−0.452	−0.456	−0.638					
Factor 5	Te	Se	Co	Au								
	0.368	0.317	−0.659	−0.554								
Factor 6	Se	Ge	Si	Cu	Sr	As	Ca	P	Al	Ti	Sn	
	0.573	0.494	0.403	0.389	0.371	0.326	0.306	0.302	−0.358	−0.438	−0.500	

Factor 3 is responsible for 12.1% of the variability and reflects the absorption of REEs, Pb and V on the IOHs. Silver and Cd are related to residual Zn sulfides. Factor 4 (10%) reflects the assemblage of aragonite (Ca, Sr), opal and atacamite (Cu) and relict Cu sulfides (Cu, Bi, Te, Au). Factor 5 explains 8.4% of the variability and exhibits positive loadings for Se and Te, which can occur in native form under low pH conditions favorable for the leaching of cobaltite. Factor 6 is probably related to coeval authigenic atacamite, opal, native selenium, aragonite, and some phosphates and arsenates. The REEs, which are related to several factors, are considered to be the elements with dual behavior.

Six TEAs for the IOHs of the Pobeda-1 hydrothermal field are identified on the basis of R-mode factor analysis (Figure 4). Negative scores reflect an increasing role of seawater products. In the Factor 1–Factor 2 plot (Figure 4a), TEA-1 represents the TEs inherited from relict chalcopyrite and isocubanite replaced by bornite, digenite, geerite, covellite and atacamite. Tin, Bi, Se, Te and Au can be incorporated in the structure of Cu–Fe sulfide or represent nanoinclusions of tellurobismuthite and native gold. TEA-II is typical of relict Zn sulfides (Zn, Cd, Tl, Ag) interacted with seawater (U, Mg, Ni, Na, K and Mo).

TEA-III reflects the intergrowths of aragonite (Ca, Sr), opal and  $\text{PO}_4^{2-}$  and  $\text{AsO}_4^{2-}$ -bearing goethite. TEA-IV encloses elements derived from clays (Al, Ga, Ti, Ge, Cr, W), barite and Mn oxyhydroxides (Ba, Mn, Co). TEA-V is closely associated with REE-bearing TEA-VI; probably reflecting the synchronous scavenging of these elements by IOHs.

The TEAs in other plots are similar to those in the Factor 1–Factor 2 plot, with some exceptions. It is suggested that Factor 3 reflects the presence of clays (Al, Ti, Cr, REEs) in IOHs (Figure 4b,c). Factor-4 is probably responsible for the chemical authigenesis in oxygenated seawater, providing a close association between barite and Mn oxyhydroxides (Mn, Co) with REEs. Another example is the assemblage of aragonite with P and As oxyanions scavenged by the IOHs (Figure 4d).

It is noteworthy that Eu occupies different positions in the plots: it is either associated with V and Pb (TEA-V, Figure 4b) close to other REEs, meaning the same manner of their accumulation, or occurs in TEA-II (Figure 4c,d), which is probably related to the halmyrolysis of Zn sulfides.

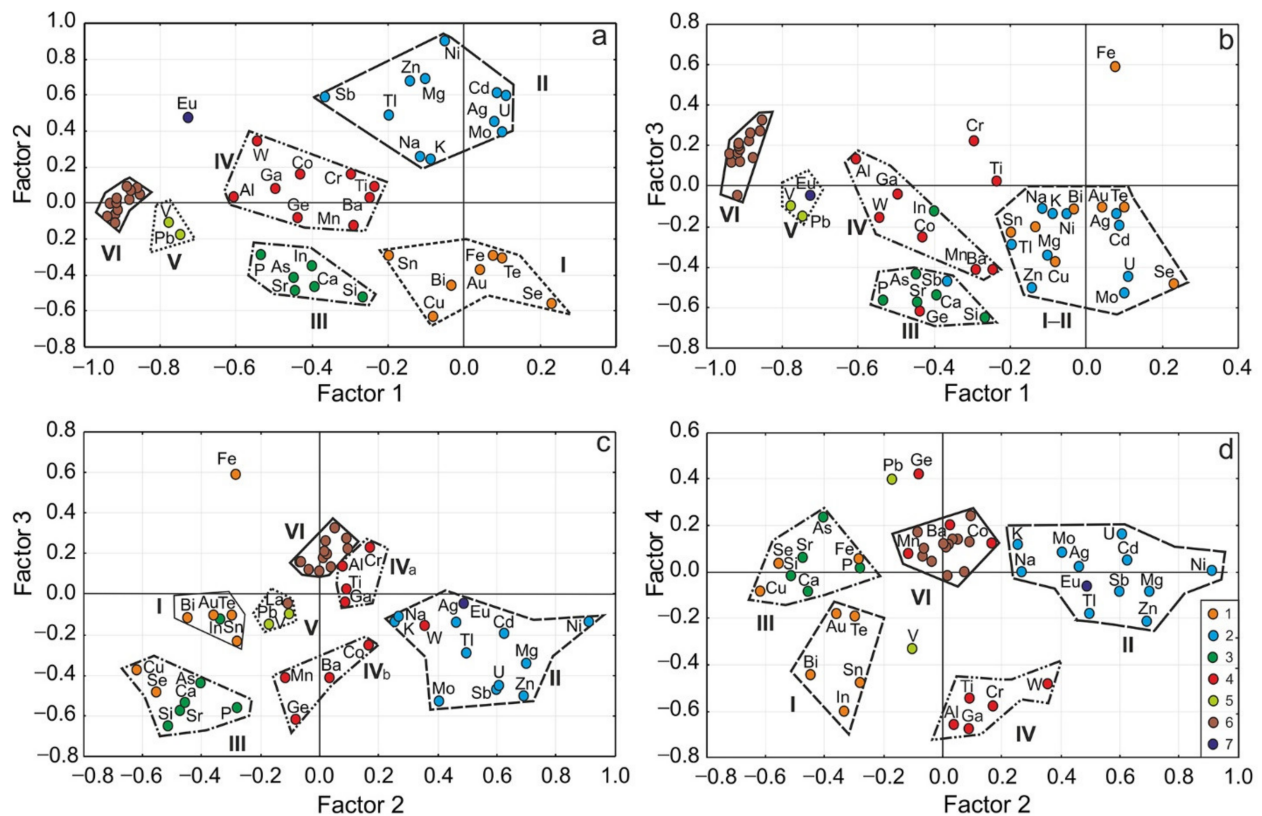


**Figure 4.** Trace element assemblages calculated for the IOHs of the Pobeda-1 hydrothermal field by R-mode factor correlations: (a,b) Factor 1 vs. Factor 2 and 3; (c,d) Factor 2 vs. 3 and 4. Rotation: Unrotated. Extraction: Principal components. TEs of: 1—Cu–Fe sulfides; 2—Zn sulfides interacted with seawater; 3—opal–aragonite mineral assemblage and  $\text{PO}_4^{2-}$ - and  $\text{AsO}_4^{2-}$ -bearing goethite; 4—clays, barite and Mn oxyhydroxides; 5 and 6—Pb, V (5) and REE (6) synchronous scavenging by IOHs; 7—Eu.

## 5. Discussion

### 5.1. General Remarks

Few data are available on the contents of selected TEs (e.g., Au, U, REEs, Cu, Zn, Se, Au, Cu, Sb, Co, P, V) in seafloor IOHs [2,21,23–26,32–34]. In this paper, we consider the widest range of TEs to assess their concentrations and assemblages in different IOH types.

In the Pobeda-1 hydrothermal field, the supergene sulfides have elevated contents of Na, K, Mg, Ni, U, Mo, V, W and Al in comparison with primary hydrothermal varieties. In comparison with hydrothermal and supergene sulfides, the IOHs also have the highest contents of these elements, as well as Au, Sr, Si, Ca, As, P and Cr. Selenium, Te and Bi exhibit similar concentrations in supergene sulfides and IOHs. Gossans are commonly considered a sink for economic metals such as Pb, Cu, Zn, Ag and Au via adsorption and coprecipitation [63,64]. In the IOHs of the Pobeda-1 hydrothermal field, the high contents of Cu (1–5 wt%), Au (0.2–32 ppm with an average of 2 ppm) and Mo (0.05–0.25 wt%) may be interesting for mining processes. The REE contents of the IOHs are higher in comparison with sulfides but are too low to be discussed from the economic viewpoint. The contents of some toxic elements (Co, Ni, Zn, As, Cd and Ag) decrease in a range from sulfides to the IOHs.

The high positive correlation of REEs with P, As, V and Pb is most likely related to the presence of arsenate, vanadate and phosphate groups in the IOHs. The high positive correlation of REEs with Al in addition to its positive correlation with clay-related TEs (Ga, Cr, Ti, W) indicates a dual occurrence of REEs. A strong positive correlation for Ca and Sr

and their weak correlation with REEs are characteristic of aragonite [38]. Copper, Se, Sn and Bi are typical of chalcopyrite, ISS and bornite [18,19].

In Zn sulfides, Zn, Cd, Sb, Ag, Tl, Cd and Ga isomorphically substitute each other, while Mg, U, Mo, W and Ni are seawater-derived elements typical of supergene sulfides intergrown with sphalerite (Table 1). A specific position of Eu apart from other REEs is probably due to the predominance of a hydrothermal sphalerite. The correlations between Bi, Te, Au, Sn, In, Cu and Se are characteristic of chalcopyrite–ISS microinclusions [18,19,65]. The positive Mn–Co correlation probably reflects their joint precipitation from seawater diluted by hydrothermal fluids [38].

The combination of various statistical methods yields the results, which are useful for the interpretations and deciphering of TEAs. Below, we discuss in detail six TEAs, which are based on the results of R-mode factor analysis.

### 5.2. TEA-I: Cu, Se, Te, Bi, Sn, Au ± In

The mineralogy and geochemistry of sulfides can change via submarine weathering [1,9,66]. Under an oxygenated seawater environment, the sulfides are oxidized into gossans, which contain IOHs, covellite, paratacamite/atacamite and chalcantite enriched with heavy metals. Supergene digenite–covellite–gererite and sphalerite–bornite aggregates, as well as relict chalcopyrite and isocubanite, in addition to atacamite, are revealed in IOHs of the Pobeda-1 hydrothermal field [17,35,49,50].

Bornite is commonly considered to be an oxidation product of primary chalcopyrite in black smoker chimneys [67,68]. The Cu-rich supergene sulfides and bornite are partly transformed into atacamite [25,69,70]. The positive correlation of Cu with In, Sn, Te and Se is attributed to their preferential incorporation into the crystal lattice of chalcopyrite or ISS formed under elevated temperature [5]. These elements were inherited by secondary Cu sulfides (Table 1). The Se/Cu ratios, however, are too high to be explained by the presence of chalcopyrite or other Cu sulfides only (Figure 5a); thus, Se probably occurs in native form too. The oxidized pyrite can be an additional source of Se [71]. The high Cu and Se concentrations in Au-rich gossans from the TAG hydrothermal field are similar to those in secondary sulfides (digenite, covellite), indicating the inheritance of this geochemical signature from primary sulfides [36]. Selenides are also common minerals for submarine and continental gossans [39,40].

The positive Bi–Te correlation is common for the chalcopyrite–isocubanite assemblage, although the presence of tellurobismuthite inclusions cannot be excluded [65,72]. In spite of a positive Bi–Te correlation, the Te/Bi ratio is much higher than that of tellurobismuthite and lower than that of the ISS, and the data points are grouped around the Te/Bi ratio line of Cu sulfides (Figure 5). A broad dispersion of Bi and Te contents suggests a dual nature of these elements (Figure 5b).

A strong positive correlation is calculated for Sn and In (Table 2, Figure 5d). The high Sn contents were determined in chalcopyrite and sphalerite from some modern hydrothermal fields associated with ultramafic rocks (up to 2210 ppm) [73]. In the Logatchev hydrothermal field, the high Sn contents are mostly typical of sphalerite (3–5 wt%) and chalcopyrite (1–2 wt%) from a high-temperature zone of smoker chimneys. The highest Sn content is detected along the replacement front of sphalerite by chalcopyrite indicating the possible occurrence of stannite inclusions [73]. Cassiterite was found in chimneys of the Dergamysh serpentinite-hosted massive sulfide deposit in the South Urals [65]. The occurrence of In in different TEAs suggests its different origins (Figures 4 and 5d).

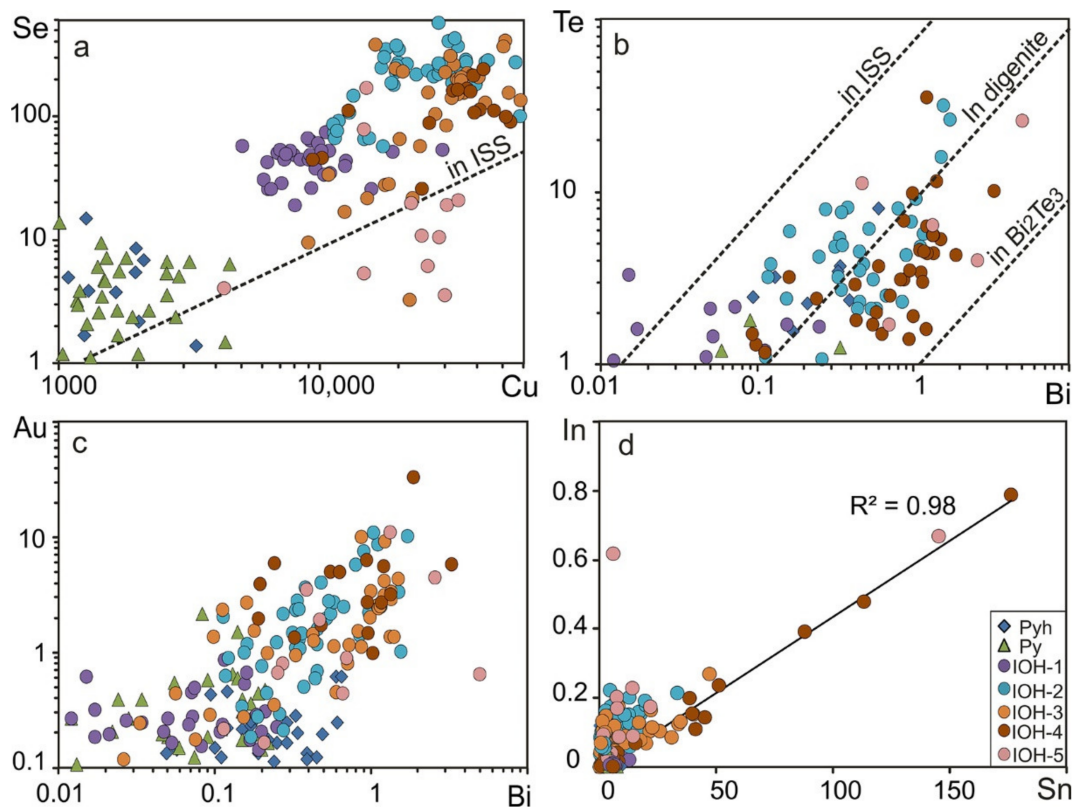


**Figure 5.** Bivariate plots of: (a) Cu vs. Se; (b) Bi vs. Te; (c) Bi vs. Au and (d) Sn vs. In for iron oxyhydroxides (IOH), pyrite (Py) and pyrrhotite (Pyh) of the Pobeda-1 hydrothermal field (ppm).

Abundant native gold was found in sulfides, cobaltite and IOHs of the Pobeda-1 hydrothermal field [35]. The Au contents increase in a range from primary hydrothermal to supergene sulfides (Table 1) similar to supergene sulfides of the Semenov-2 hydrothermal field, MAR [74]. Slightly higher Au contents are determined for the immature IOH-1 pseudomorphs formed after pyrrhotite crystals (Table 1). The crystalline IOHs replaced pyrrhotite crystals and pyrite–pyrrhotite–ISS aggregates and have elevated Au contents (up to 10.7 ppm). The maximum Au contents (up to 32 ppm) are characteristic of the IOH pseudomorphs after the isocubanite–wurtzite intergrowths, which have very low Au contents (Table 1 and Table S2). A positive correlation of Au with Bi and Te (Figure 4) suggests the association of native gold with relict Bi tellurides as in the Semenov-2 hydrothermal field [20,22,72]. The local enrichment in Au may be due to the seafloor oxidation of sulfides: for instance, Au in the IOHs from oxidized chimneys of the Snake Pit hydrothermal field; here, MAR is concentrated by a factor of three [75]. Despite the positive Au–Bi correlation, a broad dispersion of their contents suggests a dual nature of the elements (Figure 5c).

### 5.3. TEA-II: Cd, Zn, Sb, Tl, Ag, Mg, U, Mo, Ni, Na, K ± Eu

This TEA is especially characteristic of the immature IOH-1 (Figure 6a–f). A positive correlation of Zn with Cd, Sb, Tl and Ag is attributed to isomorphous lattice substitutions in relict Zn sulfides [76]. The elevated Mg, U, Mo, Na, K and Ni contents are typical of supergene sphalerite–bornite, digenite and IOH aggregates (Table 1). The high-temperature hydrothermal fluids are typically depleted in Mg [77]; thus, the relative enrichment of supergene sulfides and IOHs in Mg suggests seawater incursion into mineral aggregates. It is suggested that U, Mo, Na and K are seawater-derived elements.

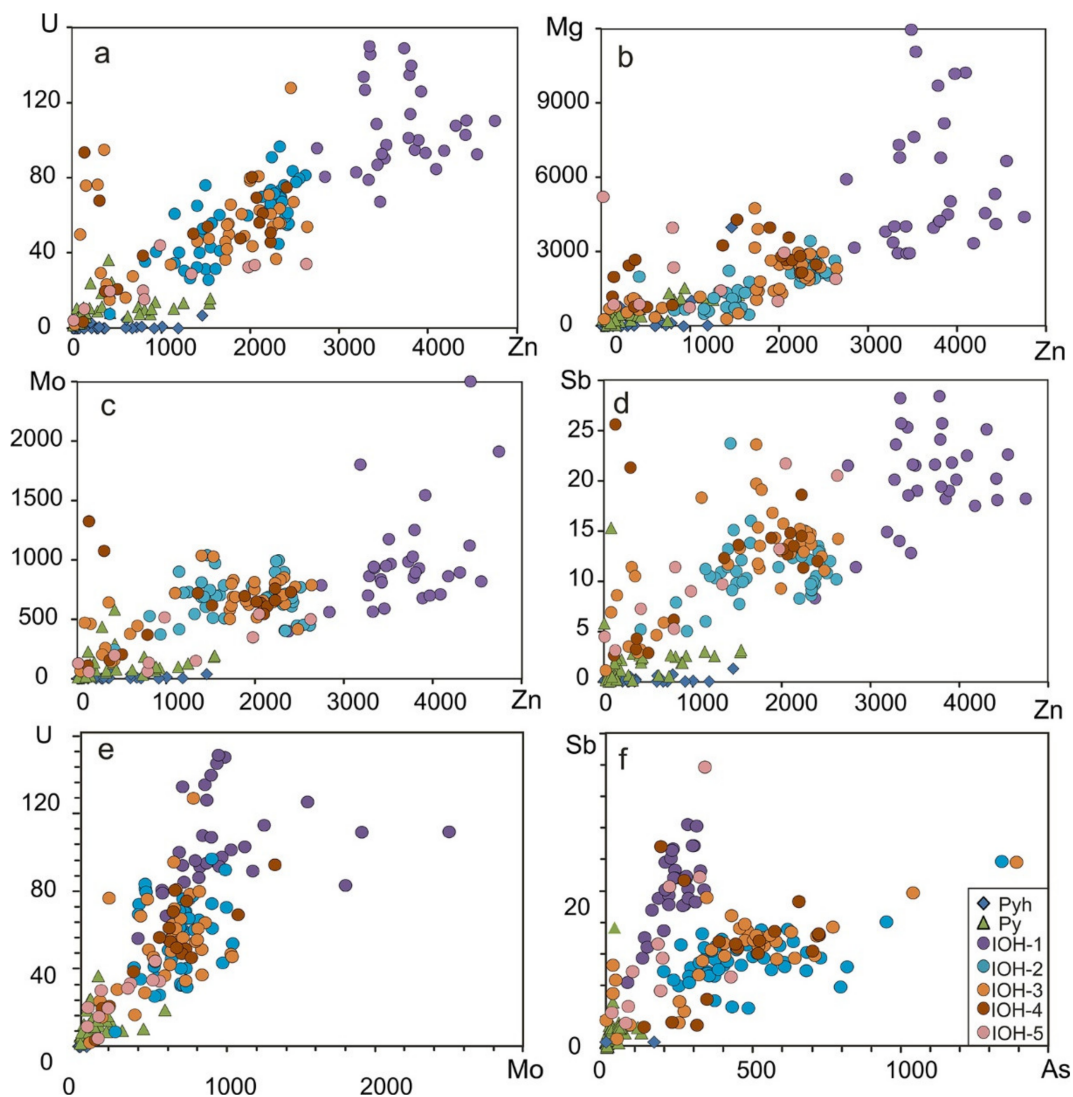


**Figure 6.** Bivariate plots of: (a) Zn vs. U; (b) Zn vs. Mg; (c) Zn vs. Mo; (d) Zn vs. Sb; (e) Mo vs. U and (f) As vs. Sb for iron oxyhydroxides (IOH), pyrite (Py) and pyrrhotite (Pyh) of the Pobeda-1 hydrothermal field (ppm).

Hydrothermal fluids venting at the seafloor are depleted in U, and pristine hydrothermal sulfides derived from these fluids have low U contents [23]. The oxidative alteration of sulfides results in the accumulation of U [78]. In our case, U is probably concomitant with Zn sulfides. It is unlikely that U is incorporated into a sphalerite lattice. Uranium enrichment via reductive processes is common in anoxic environments because the reduction of U(V) to U(IV) produces a particle-active, insoluble species [78]. In the outer wall of the black smoker chimneys, the enrichment in seawater-derived U is considered to be as a result of the redox mobilization of U(VI) to U(IV) on the oxidizing sulfide surfaces under coeval reducing conditions [5]. The U mineralization was revealed in cracks of pyrite at the Pobeda hydrothermal fields [35]. Uraninite ( $\text{UO}_2$ ) was found in modern seafloor gossans and their ancient counterparts (gossanites) from the VHMS deposits [26].

Previously, the enrichment in P and U on the surface of pyrite grains from the TAG hydrothermal field was interpreted as a signature of microbially-mediated accumulation of U in metalliferous sediments [23]. Xenotime  $\text{YPO}_4$  or ningyoite  $(\text{U,Ca,REE})_2(\text{PO}_4)_2 \cdot 1-2\text{H}_2\text{O}$  are also considered possible carriers of these elements [23]. The elevated P and U contents relative to sulfides are documented in IOHs; however, no positive correlation of U and P or U and REEs is calculated (Table 2 and Table S2). Thus, xenotime can be excluded as

a U carrier. The contents of U, as well as other associated elements, decrease in a range from IOH-1 to IOH-5 (Table 1). This is consistent with data that shows U enrichment is associated with the surfaces of the oxide–sulfide boundary and is atypical of fully oxidized mound-derived sediments [23]. It is explained by temporal reductive fixation as U(IV) in sulfide-bearing immature IOHs and its remobilization again to the soluble form U(VI) at the end of halmyrolysis.

Hydrothermal minerals, such as pyrrhotite, ISS, wurtzite and euhedral pyrite, demonstrate low contents of Mo, as well as U, in contrast to supergene digenite and sphalerite–bornite and IOH aggregates. Molybdenum is relatively abundant in seawater and is removed from seawater to sediments by a redox mechanism [23,79]. The Ni contents are low in hydrothermal pyrrhotite, wurtzite and ISS and are higher in supergene sulfides and hydrothermal euhedral pyrite compared to subhedral pyrite. In the IOHs, a positive correlation of Ni with Mg, U and Mo (Table S3) suggests an influence of seawater on its accumulation. Other elements, such as Na and K, can penetrate to pores of IOHs with hydrothermal fluids and seawater, as well.

Europium is concentrated in immature IOH-1 together with Zn, Sb and Cd. At low temperature and pH, Eu can fractionate from other REEs by selective reduction to a divalent state:  $\text{Eu}^{3+} + \text{SO}_4^{2-} + e = \text{EuSO}_4$  [80]. This local reducing condition may occur on the surface of the oxidized sulfides [5]. The elevated Eu contents are consistent with elements from three TEAs: Zn, Cd, Sb (Zn sulfides), Al, Ga, W (clays) and P and V (absorption on IOHs). This suggests a diverse nature of Eu.

#### 5.4. TEA-III: Al, Ga, Ti, W, Cr ± Ge ± (Mn, Co, Ba)

The Al contents of IOHs are much higher in comparison with those of sulfides. They increase in a range from IOH-1 to IOH-5 with increasing porous space (IOH-4) and IOH-5 mixed with clays (Table 1). The Al–Ga correlation (Table 2 and Table S2) suggests that these TEs are related to the presence of clay minerals (Figure 7a–d). It is well known that  $\text{Ga}^{3+}$  substitutes for  $\text{Al}^{3+}$  in silicates; in particular, Al-poor saponite [81,82]. These elements, however, have no positive correlation with Si, because the latter also occurs in the form of opal (Table S2). Aluminum and Ga can also be absorbed by IOHs or substituted for  $\text{Fe}^{3+}$  in goethite [83]. These elements could extensively be scavenged by IOHs from hydrothermal fluids and seawater [84]. The Ga content of wurtzite and supergene sphalerite–bornite and digenite–covellite intergrowths is higher than that of IOHs (Table 1). Some pyrite and IOH pseudomorphs inherit low Ga contents from pyrrhotite. The elevated Ge contents of IOHs are also provided by sulfides (Table 1).

In IOHs, Mn is most likely inherited from Mn-rich pseudomorphic pyrite (Py-p) (Table 1 and Table S1). The positive Mn–Co correlation is characteristic of IOHs. Cobalt, in contrast to Ni, is bounded to Mn by co-oxidation [85,86].

In natural settings, barite can precipitate by the *addition of sulfate to a Ba-rich fluid* or, vice versa, the addition of Ba to sulfate-rich seawater [87]. In our case, the oxidation of sulfides results in an increasing amount of  $\text{SO}_4^{2-}$  anions, which are precipitated in the form of barite.

The W contents increase in a range from sulfides to IOHs (Table 1). Tungsten has a positive correlation with Al and Ga that can reflect a clay source or the coeval absorption of these elements on IOHs [83,88]. On the other hand, the strong positive correlations of W with Zn, V and Sb (Table S3) suggest that W, as well as V, and probably Sb, are also absorbed on the surface of oxidizing Zn sulfides [5].

The Cr content of IOHs is higher in comparison with that of sulfides (Table 1). The Cr content increases in a range from IOH-1 to IOH-5. Chromium has much stronger positive links with Al, Ga, V, W, and Ti, which are contained in a clay component of IOHs (Table S2). It can also be absorbed by IOHs from seawater under reducing conditions [89].

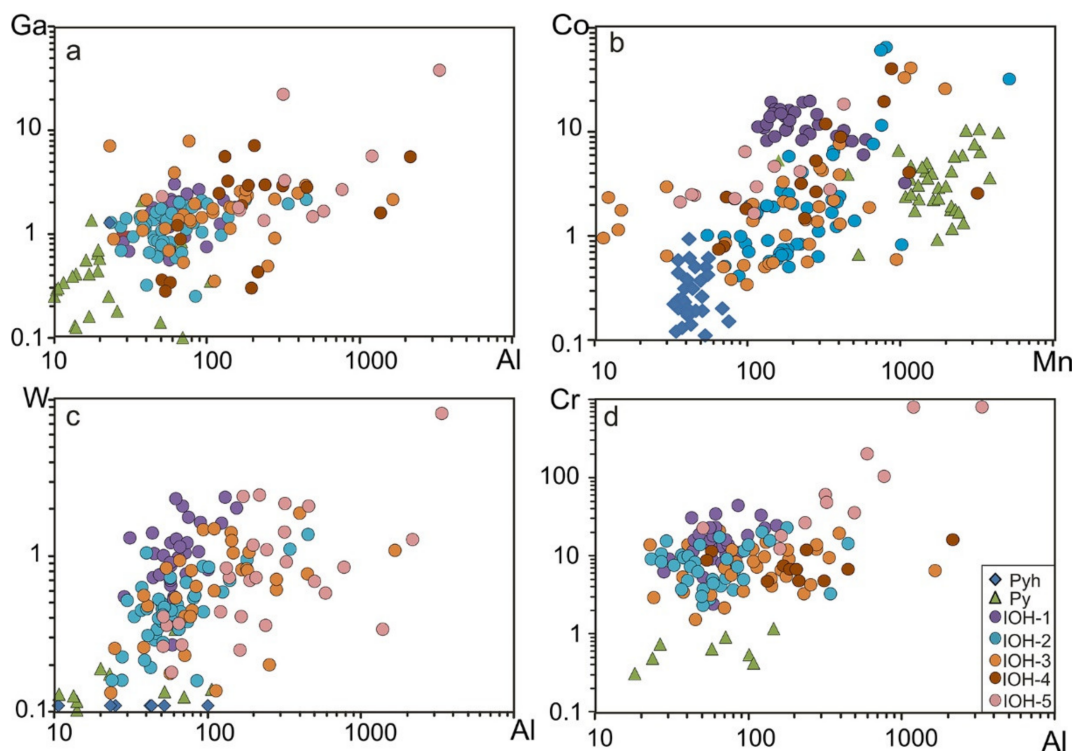


**Figure 7.** Bivariate plots of: (a) Al vs. Ga; (b) Mn vs. Co; (c) Al vs. W and (d) Al vs. Cr for the iron oxyhydroxides (IOH), pyrite (Py) and pyrrhotite (Pyh) of the Pobeda-1 hydrothermal field (ppm).

The hydrothermal and supergene sulfides, except for pyrrhotite and pyrite pseudomorphs after pyrrhotite, have elevated Ti contents (Table 1). The IOH pseudomorphs after pyrrhotite have low Ti contents. The Ti contents increase in IOH-5 with clay and various goethite fragments.

#### 5.5. TEA-IV: Ca, Sr, As, P ± Cu, Se, Si

These elements demonstrate a strong positive correlation (Table S3) and their contents form wide areas on correlation diagrams (Figure 8a–d). A strong positive Ca–Sr correlation could be related to the presence of aragonite or biogenic apatite [38]. In a weathering zone, Sr is derived from seawater and absorbed on the surface of secondary minerals and amorphous IOHs [90].

A P–As correlation is not occasional, because  $P^{5+}$  and  $As^{5+}$  are tetrahedrally coordinated by oxygen, have the same electronic configuration, and show the analogous chemical speciation in an aqueous solution. These elements, in forms of  $PO_4^{2-}$  and  $AsO_4^{2-}$ , can substitute each other in chemogenic apatite. The IOHs, however, with their large surface area, are also known as potential absorbers of arsenates and phosphates [91]. It has repeatedly been noted that the hydrothermal IOHs play a huge role in geochemical cycles of oxyanion elements such as P, As and V [29,38,92–94].

The composition of the IOHs in the Ca–P plot is broadly dispersed, and is restricted by the composition of natural Ca–Fe hydroxyphosphates, which are widespread in the IOHs of metalliferous sediments [38,95]. The Ca–Fe hydroxyphosphates have elevated Sr contents (up to 1.08 wt%), while chemogenic apatite has a low Sr content (<0.1 wt%) [38].

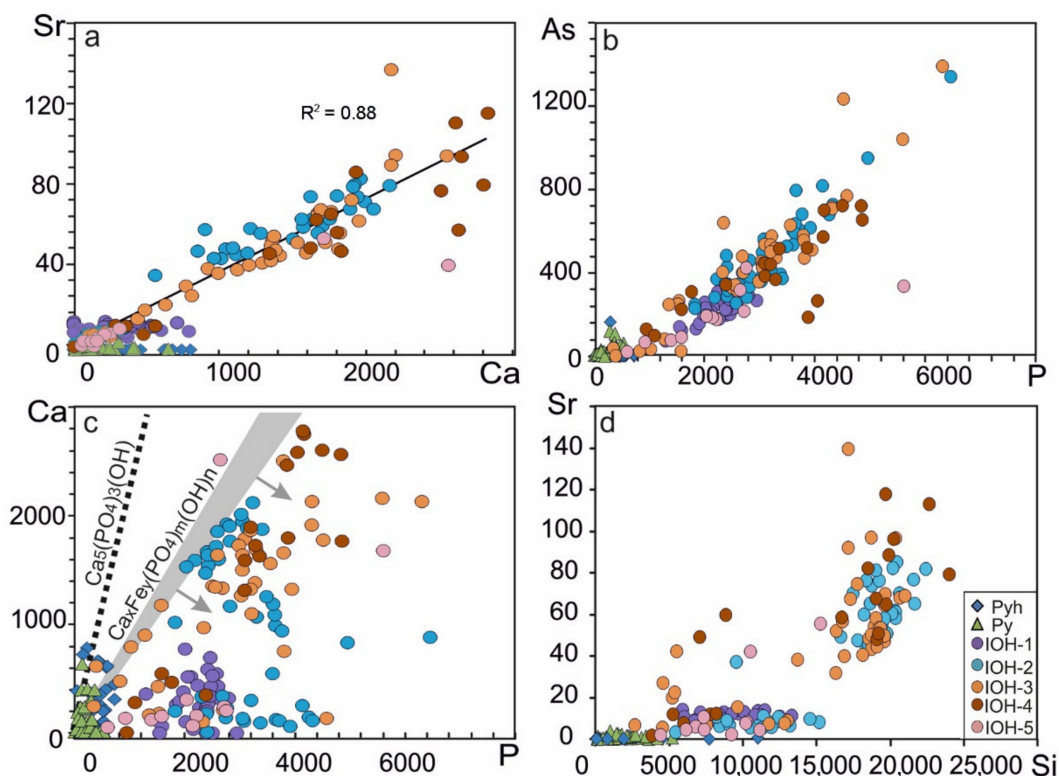


**Figure 8.** Bivariate plots of: (a) Ca vs. Sr; (b) P vs. As; (c) P vs. Ca; and (d) Si vs. Sr for the iron oxyhydroxides (IOH), pyrite (Py) and pyrrhotite (Pyh) of the Pobeda-1 hydrothermal field (ppm).

After the complete oxidation of sulfides, Cu is associated with Si, Ca, Sr, As and P in TEA-III (Figure 4c,d). In gossans, the main volume of Cu is present in the form of atacamite and paratacamite [25]. Atacamite is widespread in metalliferous sediments at the Pobeda hydrothermal field [35]. A strong positive correlation of Se with Si, Cu, Ca and Sr could indicate that part of Se, probably in invisible native form, is intergrown with atacamite, opal and aragonite in IOHs.

The IOHs contain minor Si (Table S2). The oxidation of sulfides leads to a decrease in pH. It is suggested that the local low pH is favorable for the precipitation of silica from seawater.

#### 5.6. TEAs-V: Pb, V ± REE

The V contents increase in a range from sulfides to IOHs, whereas the behavior of Pb is more complex (Table 1). Their weak correlation probably indicates a dual source of these elements (Figure 9a,b). In IOHs, Pb can be inherited from sulfides or derived from seawater [89]. It was previously envisaged that V, as well as U, is a product of seawater incursion and pyrite or galena oxidation, and these elements are fixed on sulfide surfaces under prevailing reducing conditions [5]. In our case, V, however, shows no positive correlation with U and Mo, because part of V is probably related to the clay component or V has a different style of concentration, whereas Mo and U are absorbed on Zn sulfides (Figure 9c,d). Probably,  $\text{VO}_4^{3-}$  is precipitated from seawater together with trivalent cations such as REEs or  $\text{Co}^{3+}$ ,  $\text{Al}^{3+}$  and  $\text{Ga}^{3+}$ . This idea is confirmed by a strong positive correlation of V with these elements (Table S3). Interaction with  $\text{Fe}^{3+}$  can lead to the formation of an  $\text{FeVO}_4 \cdot 1.5\text{H}_2\text{O}$  phase, which is similar to the mineral fervanite [96]. The positive correlation V with P and As may suggest a similar behavior of  $\text{VO}_4^{3-}$ ,  $\text{AsO}_4^{3-}$  and  $\text{PO}_4^{3-}$ .

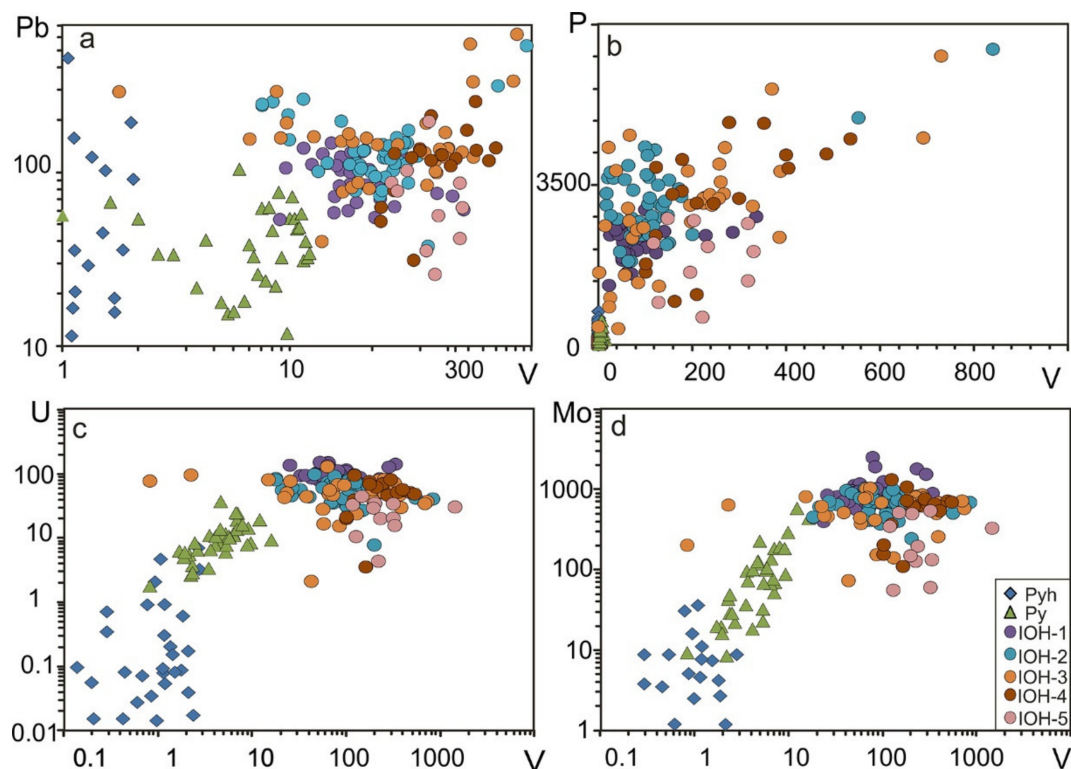


**Figure 9.** Bivariate plots of: (a) V vs. Pb; (b) V vs. P; (c) V vs. U and (d) V vs. Mo for the iron oxyhydroxides (IOH), pyrite (Py) and pyrrhotite (Pyh) of the Pobeda-1 hydrothermal field (ppm).

### 5.7. TEAs VI: REEs ± Mn, Co, Ba

The REEs are powerful tracers in the study of the evolution of geochemical systems and are widely used to identify the sources of oceanic REEs and mixing processes within the oceans and hydrothermal-sedimentary systems [97]; in particular, the contribution from hydrothermal fluids and seawater [24,32,38,98]. The REEs occur in a trivalent state in most natural conditions and behave in a chemically coherent manner. The exceptions are Ce and Eu, which can behave anomalously under certain redox conditions due to the formation of  $Ce^{4+}$  and  $Eu^{2+}$  species [24].

In our study, sulfides show very low REE contents close to or below the DL of the LA-ICP-MS analysis in contrast to IOHs (Table S3). This is consistent with data that shows the REE contents of IOHs are higher by two orders of magnitude than those of sulfides [24,38]. All IOH phases from the Pobeda-1 hydrothermal field show positive Eu and negative Ce anomalies when normalized to chondrite or NASC REE values (Figure 10a,b). The negative Ce anomaly is probably a result of the absorption of REEs on IOHs from seawater, while the positive Eu anomaly indicates the contribution from a hydrothermal source [24,32,38,98]. Because of the positive correlations between all REEs and P, V and As, it is suggested that the REEs can also be precipitated together with  $PO_4^{3-}$ ,  $VO_4^{3-}$  and  $AsO_4^{3-}$  complexes. The Fe–Ca hydroxophosphates are enriched in REEs except for Ce, which consequently demonstrates a negative anomaly [38].

A pronounced seawater-normalized REE pattern of IOHs, however, exhibits a positive Ce anomaly (Figure 9c). The excess of Ce probably reflects its precipitation as  $CeO_2$ . The behavior of Ce in seawater is similar to Ti, which is supported by a positive Ce–Ti correlation in our IOHs. The positive correlations of Ce with Al, Ti and W indicate that the excess of Ce is probably due to the contamination of the IOHs by a minor amount of clay.

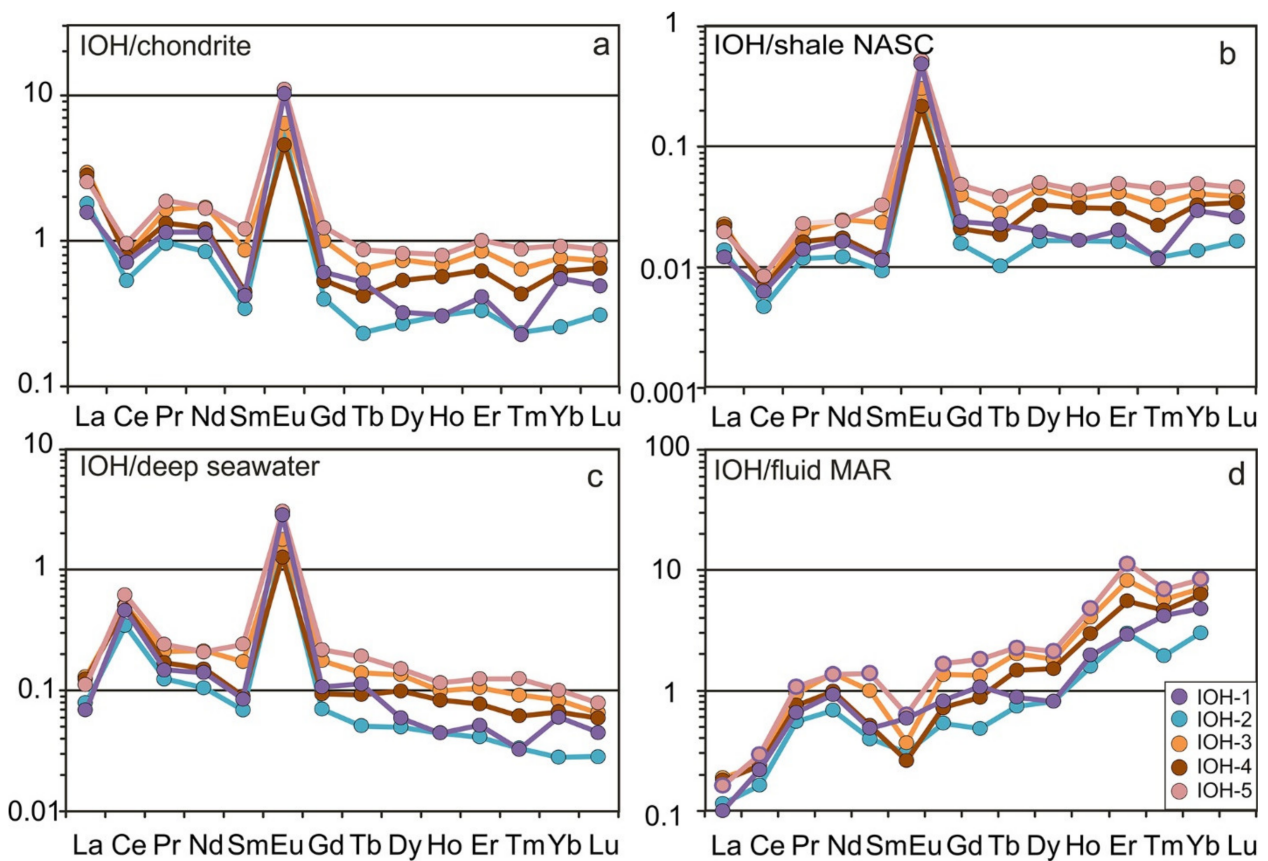


**Figure 10.** REE patterns of the IOHs of the Pobeda-1 hydrothermal field normalized to: (a) chondrite [99], (b) NASC [92], (c) deep seawater [100], and hydrothermal fluids of the MAR ultramafic-hosted Rainbow (brown lines), and (d) basalt-hosted Broken Spur, Snake Pit, Lucky Strike and TAG hydrothermal fields (green lines) [38].

Little or no fractionation between LREEs and HREEs is observed in IOHs of the Pobeda-1 hydrothermal field. The IOH types are characterized by a more prominent enrichment in HREEs when normalized to the composition of high-temperature hydrothermal fluids of the MAR hydrothermal fields (Figure 10d).

The idea of a hydrothermal nature of the Eu anomaly is equivocal. In hydrothermal solutions under high temperatures and pressures, Eu mostly occurs in a divalent state, hence  $\text{Eu}^{2+}$  is stronger when complexed with chloride and much more stable than other REEs(III) [101]. A large amount of sulfate may scavenge  $\text{Eu}^{2+}$  and precipitate as an insoluble  $\text{EuSO}_4$  at low temperatures [102]. However,  $\text{Eu}^{2+}$  is easily oxidized to  $\text{Eu}^{3+}$  in oxygenated seawater and the Eu anomaly will be diminished [103]. In this case, Eu can fractionate from other REEs as insoluble  $\text{EuSO}_4$  at low temperature and pH (see TEAs-2). These local reducing conditions may occur on the surface of the oxidized sulfides [5].

The porous and clastic IOHs are characterized by positive correlations between Eu, V, Al and Pb (Figure 11). A hydrothermal source of REEs, and especially Eu, cannot be confirmed by a positive correlation with these elements because they could be derived from hydrothermal fluid, seawater and clays [27,38,89].

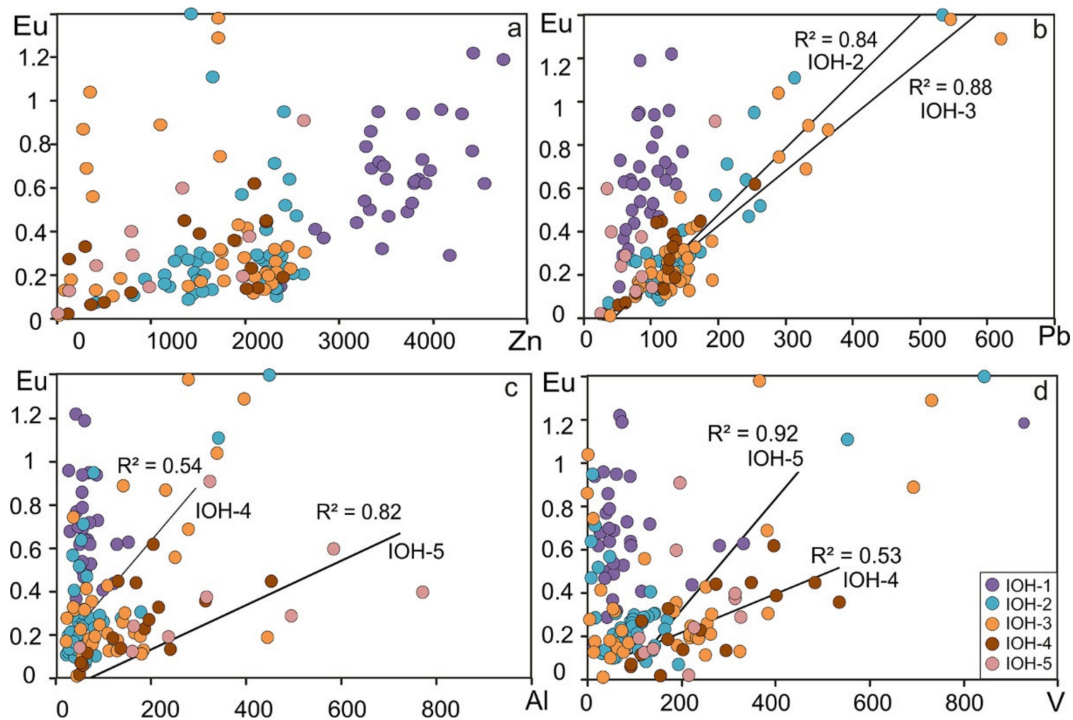


**Figure 11.** Bivariate plots of: (a) Zn vs. Eu; (b) Pb vs. Eu; (c) Al vs. Eu and (d) V vs. Eu for the iron oxyhydroxides (IOH) types of the Pobeda-1 hydrothermal field (ppm).

### 5.8. General Model

The IOHs studied mainly form as a result of the in situ seafloor oxidation (halmyrolysis) of sulfides. The IOHs are devoid of laminated textures of hydrothermal-sedimentary particles. Adjacent clastic fragments testify to seafloor oxidation as well. The halmyrolysis includes two main stages: (1) the oxidation of sulfur of hydrothermal sulfides and the formation of secondary sulfides, and (2) the oxidation of Fe(II) of secondary sulfides and the dissolution of chalcogenides. All these processes are accompanied by the absorption of TEs from ambient seawater, locally, and mixed with those from hydrothermal fluids.

At the first stage, halmyrolysis leads to the formation of supergene pyrite after pyrrhotite and bornite after isocubanite and chalcopyrite. Bornite is replaced by digenite, geerite and covellite. In TEA-1, the secondary Cu sulfides inherit the TEs, which are typical of relict hydrothermal isocubanite and chalcopyrite intergrowths (Se, Te, Au, Bi, Sn, In). Their association with Si indicates the precipitation of opal on the surfaces of oxidizing sulfides under local low pH conditions. Atacamite forms closely to this place. The high Se contents may be related to the presence of its native form. The synchronous oxidation of wurtzite-bearing pyrite–pyrrhotite aggregates leads to the formation of secondary sphalerite with TEA-2 (Figure 3). The sphalerite inherits Cd, Ag, Sb and Tl. Local reducing conditions formed on the surface of oxidizing sulfides are favorable for the U, Ni and Mo absorption from seawater. It is also suggested that  $\text{Eu}^{3+}$  is reduced to  $\text{Eu}^{2+}$  with the precipitation of insoluble  $\text{EuSO}_4$ .

At the second stage of halmyrolysis, the IOHs scavenge the TEs, which form TEAs-III, IV, V and VI. TEA-III with Al, Ge, Ga and W can reflect the presence of clays or their incorporation in the structure of IOHs. Under oxidizing conditions, the Co-rich Mn oxyhydroxides are precipitated together with barite. The latter is precipitated due to increasing sulfate contents after the oxidation of sulfides. The immature IOHs scavenge As and P of TEA-IV as oxyanions and are precipitated together with atacamite, aragonite (Ca, Sr), opal (Si) and Se. Lead and V from TEA-V are probably absorbed in IOHs from seawater together with REEs (TEA-VI).

The high content of a number of TEs in IOHs of the Pobeda-1 hydrothermal field is a result of their high scavenging capacity. The peculiarities of the TE composition indicate several sources: they can simultaneously be scavenged by IOHs from hydrothermal fluids, oxidizing sulfides, clays and seawater.

### 5.9. Comparison of IOHs from Different Hydrothermal Fields

The halmyrolysis process differ at ultramafic- and mafic-hosted hydrothermal fields, thus the distinct incorporation of TEs in the IOHs may be anticipated. The idea is revised by the TEs' comparison of the IOHs collected in the ultramafic-hosted Pobeda-1 and Rainbow and the mafic-hosted Galapagos Spreading Center (GSC at 87° W) and East Pacific Rise (EPR 9°50' N) hydrothermal fields (Tables 6 and 7). The contents of seawater-derived TEs (Na, Mg, Al, P, Ca, Sr, V, U), except for Mo, are similar in the IOHs of the Pobeda, Rainbow and GSC hydrothermal fields (Tables 6 and 7), while primary sulfides are depleted in these elements. It is interesting that the REE contents are higher in IOHs from the ultramafic-hosted hydrothermal sulfide fields than from mafic-hosted ones. This is consistent with the higher REE contents in hydrothermal fluids of the ultramafic-hosted systems in comparison with those emanated in mafic-hosted systems (Figure 10).

**Table 6.** Average contents (av) and standard deviation (sd) of IOHs of the ultramafic-hosted Pobeda-1 and Rainbow (36°14' N, MAR) hydrothermal fields, Mid-Atlantic Ridge, ppm.

SMS Site		Fe,%	Na	Mg	Al	Si	P	K	Ca	Sr	Ti	V	
Pobeda	av	56	7441	2752	152	13,526	2814	559	949	36	5.0	155	
	sd	2.6	4541	2204	262	5552	1054	475	798	31	12	143	
<i>n</i> = 140	av	19	353	7.4	19	24,495	2076	1.8	396	146	688	1.1	
	sd	70	597	14	27	13,772	1113	2,2	241	115	336	2.2	
			Cr	Mn	Co	Ni	Cu	Zn	Ga	As	Se	Mo	Ag
	av	0.2	0.10	13	14	5.8	0.5	2.1	0.6	135	64		
	sd	0.3	0,11	24	5.9	6.7	0.5	3.4	0.6	89	32		
Rainbow	av	60	11,888	972	290	17,527	2553	625	1695	41	3.0	295	
	sd	2.4	3991	411	916	5746	923	476	5052	55	3.3	146	
<i>n</i> = 56	av	19	1083	1739	6	259	15,453	0.4	172	14	23	1.1	
	sd	15	558	1074	3	765	11,505	0.2	78	93	24	2.7	
			Cr	Mn	Co	Ni	Cu	Zn	Ga	As	Se	Mo	Ag
	av	4.7	0.02	0.7	2.8	20	3.5	DL	3.7	502	5.9		
	sd	4.3	0.02	1.0	1.0	19	2.3		5.0	556	2.6		

The IOHs of the same samples of the ultramafic-related Rainbow hydrothermal field have much higher Co contents than the IOHs of the Pobeda-1 hydrothermal field (Table 6). These dramatic differences are explained by the distinct composition of primary sulfides. The relict colloform pyrite in IOHs of the Rainbow chimneys is Co-rich (av. 717 ppm). In the Pobeda-1 hydrothermal field, pyrrhotite and pseudomorphic pyrite after pyrrhotite (Py-*p*) replaced by IOHs have low contents of Co, while Co-rich euhedral pyrite is still preserved in the samples studied (Table 1). In the Rainbow hydrothermal field, the pyrite with low Co contents is replaced by Co-poor IOHs. A similar consistent pattern is recognized in the mafic-hosted GSC hydrothermal field, where the Co contents of IOHs (av. 3 ppm) and primary pyrite (av. 0.1 ppm) are similar. On the other hand, the pyrite-pyrrhotite aggregates in chimneys of the EPR 9°50' N hydrothermal field (76–6075 ppm) are consistent with the average Co contents of IOHs of 5.8 ppm and 1739 ppm, respectively [104]. The Co-poor pyrrhotite of the Pobeda-1 hydrothermal field was replaced by IOHs with low Co contents (Table 1). In general, the Co and Cr contents of IOHs are often higher than those of primary pyrite: for instance, 2–8 ppm Co and 32 ppm Cr in IOHs of the mafic-hosted

Broken Spur chimneys in contrast to 2–8 ppm Co and 1 ppm Cr contents of primary pyrite, respectively [104].

In the Rainbow hydrothermal field, the Co contents decrease in the following morphogenetic IOH range: laminated (av. 1739 ppm) → pseudomorphous (av. 242 ppm) → bacteriomorphous (av. 4 ppm), similar to other hydrothermal fields studied (our unpublished data).

Thus, some features of the IOHs of the ultramafic- and mafic-hosted vent sites differ and the composition of some IOHs depends on the local physicochemical conditions for the formation of primary sulfides. Due to the complexity, this study merits further research.

**Table 7.** Average contents (av) and standard deviations (sd) of TEs in IOHs of the mafic-hosted Galapagos Spreading Center (GSC~86° W) and East Pacific Rise (EPR 9°50') hydrothermal fields in the Pacific Ocean, ppm.

GSC		Fe,%	Na	Mg	Al	Si	P	K	Ca	Sr	Ti	V	
<i>n</i> = 66	av	62	2774	840	449	10,442	3925	255	849	20	5.8	311	
	sd	0.3	981	160	805	1304	1787	174	234	6.4	10	499	
		Cr	Mn	Co	Ni	Cu	Zn	Ga	As	Se	Mo	Ag	
	av	12	154	5.8	1.0	12,811	1775	16	123	2.5	285	0.1	
	sd	10	425	13	1.4	4313	1219	26	167	1.0	404	0.1	
		Cd	In	Sn	Sb	Ba	La	Au	Tl	Pb	U		
	av	0.2	14	0.4	52	3.7	0.1	DL	0.3	424	44		
	sd	0.2	6.9	0.3	21	5.8	0.2		0.2	326	33		
	EPR 9°50' N <i>n</i> = 8		Ti	V	Cr	Mn	Fe,%	Co	Ni	Cu	Zn	As	Se
		av	19	5.2	3.0	13	62	2127	1	3798	1037	29	697
		sd	28	4.2	2.3	3.8	8197	1727	1	3592	866	39	1190
			Mo	Ag	Cd	Sn	Sb	Te	Ba	La	Tl	Pb	U
av		449	1.9	2.7	7.0	0.7	0.3	1.3	0.5	0.4	33	2.3	
sd		392	1.5	2.3	5.0	1.0	0.5	1.0	0.5	0.5	39	4.4	

## 6. Conclusions

1. In this paper, we compare the trace element (TE) composition of hydrothermal and supergene sulfides and iron oxyhydroxides (IOHs). In comparison with hydrothermal sulfides (ISS, wurtzite, subhedral and euhedral pyrite), supergene sulfides are characterized by a moderate increase in seawater-derived TEs (Na, Mg, U, Mo, Ni). The IOHs are significantly enriched in seawater-derived (Na, K, Mg, Ca, Sr, P, U, Mo, V) and residual hydrothermal (Cu, Zn, Cd, Pb, Sb, Au, Se, Bi) TEs. According to the statistical analysis, the TEs are grouped into six associations (TEAs): (I) Cu, Se, Te, Bi, In, Sn, and Au; (II) Zn, Sb, Tl, Cd, Ag, Mg, U, Mo, Cr and Ni; (III) Al, Ga, Ge, Ti, Mn, Co, Ba, W, Na and K; (IV) Ca, Sr, As, P, V and Si; (V) Pb and V; and (VI) REEs except for Eu.
2. The halmyrolysis of hydrothermal sulfides includes two stages, which can explain TE behavior. The Oxidation of hydrothermal sulfides and the formation of secondary sulfides is a characteristic process of the first stage. Pyrrhotite is replaced by pyrite and then by secondary chalcopyrite. The hydrothermal chalcopyrite–isocubanite aggregates and secondary chalcopyrite are transformed into bornite and Cu sulfides. Wurtzite is replaced by secondary sphalerite in assemblage with secondary Cu sulfides. The relict sulfides inherit the TEs from primary sulfides (TEA-I and TEA-II). The oxidation of primary sulfides provides local low pH reducing conditions, which are necessary both for the formation of secondary sulfides and the scavenging of some redox-sensitive elements, such as U(IV), Mo (IV) and Eu (II) on these surfaces in TEA-II. Pseudomorphous Mn-bearing pyrite after pyrrhotite can be a source of Mn for other minerals.
3. The second stage of halmyrolysis is related to the oxidation of Fe(II) and the formation of IOHs under oxic conditions accompanied by the increase in pH. In TEA-III, Al,

Ge, Ga, W and Cr are probably supplied from clays and/or are incorporated in the structure of IOHs with the coeval precipitation of Mn oxyhydroxides and barite. During this stage, the authigenic atacamite (Cu), opal (Si) and aragonite (Ca, Sr) are associated with oxyanions of As and P, probably absorbed by IOHs (TEA-III). Lead and V (TEA-V) are probably absorbed from seawater together with REEs (TEA-VI).

4. There are high contents of Cu (1–5 wt%), Au (0.2–32 ppm with an average of 2 ppm) and Mo (0.05–0.25 wt%) are in the IOHs of the Poveda-1 hydrothermal field. The contents of some toxic elements (Co, Ni, Zn, As, Cd, Ag) decrease in a range from hydrothermal and supergene sulfides to IOHs.
5. Some TE features of the IOHs from the ultramafic- and mafic-hosted hydrothermal fields differ, whereas others depend on local physicochemical conditions for the formation of primary sulfides.
6. The development of the halmyrolysis model should be further elaborated in order to revise the TEs' composition of different morphogenetic IOH types in other hydrothermal fields.

**Supplementary Materials:** The following are available online at <https://www.mdpi.com/article/10.3390/min13010004/s1>, Table S1: Trace element contents and statistical parameters (mean, standard deviation, maximum, minimum, median, correlation coefficients) of sulfides of the Poveda-1 hydrothermal field; Table S2: Trace element contents and statistical parameters (mean, standard deviation, maximum, minimum, median, correlation coefficients) of iron oxyhydroxides (IOH) types of the Poveda-1 hydrothermal field; Table S3: Trace element contents and statistical parameters (mean, standard deviation, maximum, minimum, median, correlation coefficients) of all iron oxyhydroxides of the Poveda-1 hydrothermal field; Table S4: a—Factor coordinates of the variables, based on correlations, and b—Q-mode factors and their eigenvalues, variance and cumulative variance.

**Author Contributions:** V.V.M. interpreted the results and wrote the text; G.A.C., A.V.F. and V.E.B. collected samples for the study; N.R.A. and I.Y.M. revised the manuscript; D.A.A. and A.S.T. performed the LA-ICP-MS analyses; I.A.B. performed the SEM/EDS analyses. All authors have read and agreed to the published version of the manuscript.

**Funding:** The geochemical studies were supported by the Russian Science Foundation, project № 22-17-00215. The mineralogical studies were supported by state contract of IMin SU FRC MG UB RAS no. 122031600292-6.

**Acknowledgments:** The authors are sincerely grateful to the crew of the Research Vessel “Professor Logachev” for their assistance in sampling of the specimens for study during the 37th cruise.

**Conflicts of Interest:** The authors declare no conflict of interest.

## References

1. Hannington, M.D.; Thompson, G.; Rona, P.A.; Scott, S.D. Gold and native copper in supergene sulphides from the Mid-Atlantic Ridge. *Nature* **1988**, *333*, 64–66. [[CrossRef](#)]
2. Herzig, P.M.; Hannington, M.D.; Scott, S.D.; Maliotis, G.; Rona, P.A.; Thompson, G. Gold-rich sea-floor gossans in the Troodos Ophiolite and on the Mid-Atlantic Ridge. *Econ. Geol.* **1991**, *86*, 1747–1755. [[CrossRef](#)]
3. Hannington, M.D. The formation of atacamite during weathering of sulfides on the modern seafloor. *Can. Mineral.* **1993**, *31*, 945–956.
4. Halbach, P.; Blum, N.; Münch, U.; Plüger, W.; Garbe-Schönberg, D.; Zimmer, M. Formation and decay of a modern massive sulfide deposit in the Indian Ocean. *Miner. Deposita* **1998**, *33*, 302–309. [[CrossRef](#)]
5. Butler, I.B.; Nesbitt, R.W. Trace element distributions in the chalcopyrite wall of a black smoker chimney: Insights from laser ablation inductively-coupled plasma mass spectrometry (LA-ICP-MS). *Earth Planet. Sci. Lett.* **1999**, *167*, 335–345. [[CrossRef](#)]
6. Houghton, J.L.; Shanks, W.C.; Seyfried, W.E., Jr. Massive sulfide deposition and trace element remobilization in the Middle Valley sediment-hosted hydrothermal system, northern Juan de Fuca Ridge. *Geochim. Cosmochim. Acta* **2004**, *68*, 2863–2873. [[CrossRef](#)]
7. Bogdanov, Y.A.; Lein, A.Y.; Maslennikov, V.V.; Syaoli, L.; Ulyanov, A.A. Mineralogical-geochemical features of sulfide ores from the Broken Spur hydrothermal field. *Oceanology* **2008**, *48*, 679–700. [[CrossRef](#)]
8. Lein, A.Y.; Bogdanov, Y.A.; Maslennikov, V.V.; Li, S.; Ulyanova, N.V.; Maslennikova, S.P.; Ulyanov, A.A. Sulfide minerals in the Menez Gwen nonmetallic hydrothermal field (Mid-Atlantic Ridge). *Lithol. Miner. Resour.* **2010**, *45*, 305–323. [[CrossRef](#)]
9. Ridley, W.I. Weathering processes. In *Volcanogenic Massive Sulfide Occurrence Model*; Shanks, W.C., Thurston, R., Eds.; Report 2010–5070-C; U.S. Geological Survey Scientific Investigations: Reston, VA, USA, 2012; pp. 195–201.

10. Large, R.R.; Halpin, J.A.; Danyushevsky, L.V.; Maslennikov, V.V.; Bull, S.W.; Long, J.A.; Gregory, D.D.; Lounejeva, E.; Lyons, T.W.; Sack, P.J.; et al. Trace element content of sedimentary pyrite as a new proxy for deep-time ocean–atmosphere evolution. *Earth Planet. Sci. Lett.* **2014**, *389*, 209–220. [[CrossRef](#)]
11. Li, X.; Wang, J.; Chu, F.; Wang, H.; Li, Z.; Yu, X.; Bi, D.; He, Y. Variability of Fe isotope compositions of hydrothermal sulfides and oxidation products at mid-ocean ridges. *J. Mar. Syst.* **2016**, *180*, 191–196. [[CrossRef](#)]
12. Edwards, K.J. Formation and Degradation of Seafloor Hydrothermal Sulfide Deposits. *Spec. Pap. Geol. Soc. Am.* **2004**, *379*, 83–96. [[CrossRef](#)]
13. Fallon, E.K.; Niehorster, E.; Brooker, R.A.; Scott, T.B. Experimental leaching of massive sulphide from TAG active hydrothermal mound and implications for seafloor mining. *Mar. Pollut. Bull.* **2018**, *126*, 501–515. [[CrossRef](#)] [[PubMed](#)]
14. Knight, R.D.; Roberts, S.; Cooper, M.J. Investigating monomineralic and polyminerallitic reactions during the oxidation of sulphide minerals in seawater: Implications for mining seafloor massive sulphide deposits. *Appl. Geochem.* **2018**, *90*, 63–74. [[CrossRef](#)]
15. Meng, X.; Li, X.; Chu, F.; Zhu, J.; Lei, J.; Li, Z.; Wang, H.; Chen, L.; Zhu, Z. TE and sulfur isotope compositions for pyrite across the mineralization zones of a sulfide chimney from the East Pacific rise (1–2°S). *Ore Geol. Rev.* **2020**, *116*, 103203. [[CrossRef](#)]
16. Maslennikov, V.V.; Maslennikova, S.P.; Large, R.R.; Danyushevsky, L.V. Study of trace elements zonation in vent chimneys from the Silurian Yaman-Kasy volcanic-hosted massive sulfide deposit (Southern Urals, Russia) using laser ablation-inductively coupled plasma mass spectrometry (LA-ICPMS). *Econ. Geol.* **2009**, *104*, 1111–1141. [[CrossRef](#)]
17. Maslennikov, V.V.; Cherkashov, G.; Artemyev, D.A.; Firstova, A.; Large, R.R.; Tseluyko, A.; Kotlyarov, V. Pyrite Varieties at Pobeda Hydrothermal Fields, Mid-Atlantic Ridge 17°070–17°080 N: LA-ICP-MS Data Deciphering. *Minerals* **2020**, *10*, 622. [[CrossRef](#)]
18. Wohlgemuth-Ueberwasser, C.C.; Viljonen, F.; Petersen, S.; Vrster, C. Distribution and solubility limits of trace elements in hydrothermal black smoker sulfides: An in-situ LA-ICP-MS study. *Geochim. Cosmochim. Acta* **2015**, *159*, 16–41. [[CrossRef](#)]
19. Keith, M.; Hackel, F.; Haase, K.M.; Schwarz-Schampera, U.; Klemd, R. Trace elements systematics of pyrite from submarine hydrothermal vents. *Ore Geol. Rev.* **2016**, *72*, 728–745. [[CrossRef](#)]
20. Ding, T.; Wang, J.; Tao, C.H.; Dias, A.A.; Liang, J.; Wang, Y.; Chen, J.; Wu, B.; Huang, H. Trace-element compositions of sulfides from inactive Tianzuo hydrothermal field, Southwest Indian Ridge: Implications for ultramafic rocks hosting mineralization. *Ore Geol. Rev.* **2022**, *140*, 104421. [[CrossRef](#)]
21. Melekestseva, I.; Maslennikov, V.V.; Tref'yakov, G.; Maslennikova, S.P.; Danyushevsky, L.; Ross, L.; Beltenev, V.; Khvorov, A. TE geochemistry of sulfides from the Ashadze-2 hydrothermal field (12°58' N, Mid-Atlantic Ridge): Influence of host rocks formation conditions or seawater? *Minerals* **2020**, *10*, 743. [[CrossRef](#)]
22. Ayupova, N.; Melekestseva, I.; Maslennikov, V.; Sadykov, S. Mineralogy and geochemistry of clastic sulfide ores from the Talgan VHMS deposit, South Urals, Russia: Signatures of diagenetic alteration. *Ore Geol. Rev.* **2022**, *144*, 104839. [[CrossRef](#)]
23. Mills, R.A.; Thomson, J.; Elderfield, H.; Hinton, R.W.; Hyslop, E. Uranium enrichment in metalliferous sediments from the Mid-Atlantic Ridge. *Earth Planet. Sci. Lett.* **1994**, *124*, 35–47. [[CrossRef](#)]
24. Mills, R.A.; Elderfield, H. Rare earth element geochemistry of hydrothermal deposits from the active TAG Mound. 26°N Mid-Atlantic Ridge. *Geochim. Cosmochim. Acta* **1995**, *59*, 3511–3524. [[CrossRef](#)]
25. Dekov, V.; Boycheva, T.; Hålenius, U.; Petersen, S.; Billström, K.; Stummeyer, J.; Kamenov, G.; Shanks, W. Atacamite and paratacamite from the ultramafic-hosted Logatchev seafloor vent field (14°45'N, Mid-Atlantic Ridge). *Chem. Geol.* **2011**, *286*, 169–184. [[CrossRef](#)]
26. Ayupova, N.R.; Melekestseva, I.Y.; Maslennikov, V.V.; Tseluyko, A.S.; Blinov, I.A.; Beltenev, V.E. Uranium accumulation in modern and ancient Fe-oxide sediments: Examples from the Ashadze-2 hydrothermal sulfide field (Mid-Atlantic Ridge) and Yubileynoe massive sulfide deposit (South Urals, Russia). *Sediment. Geol.* **2018**, *367*, 164–174. [[CrossRef](#)]
27. Meng, X.; Jin, X.; Li, X.; Chu, F.; Zhang, W.; Wang, H.; Zhu, J.; Li, Z. Mineralogy and geochemistry of secondary minerals and oxyhydroxides from the Xunmei hydrothermal field, Southern Mid-Atlantic Ridge (26°S): Insights for metal mobilization during the oxidation of submarine sulfides. *Mar. Geol.* **2021**, *442*, 106654. [[CrossRef](#)]
28. Mitra, A.; Elderfield, H.; Greaves, M.J. Rare earth elements in submarine hydrothermal fluids and plumes from the Mid-Atlantic Ridge. *Mar. Chem.* **1994**, *47*, 217–236. [[CrossRef](#)]
29. Edmonds, H.N.; German, C.R. Particle geochemistry in the Rainbow hydrothermal plume, Mid-Atlantic Ridge. *Geochim. Cosmochim. Acta* **2004**, *68*, 759–772. [[CrossRef](#)]
30. Popoola, S.O.; Han, X.; Wang, Y.; Qiu, Z.; Ye, Y.; Cai, Y. Geochemical investigations of Fe-Si-Mn oxyhydroxides deposits in Wocan hydrothermal field on the slow-spreading Carlsberg Ridge, Indian Ocean: Constraints on their types and origin. *Minerals* **2019**, *9*, 19. [[CrossRef](#)]
31. Rusakov, V.Y.; Shilov, V.V.; Roschina, I.A.; Kononkova, N.N. Accumulation history of the metalliferous and ore-bearing sediments of the Krasnov hydrothermal field (MAR 16°38' N) for the past 80 ka BP (part I). *Geochem. Intern.* **2011**, *49*, 1208–1238. [[CrossRef](#)]
32. Barrett, T.J.; Jarvis, I.; Jarvis, K. Rare earth element geochemistry of massive sulfides-sulfates and gossans on the southern Explorer Ridge. *Geology* **1990**, *18*, 583–586. [[CrossRef](#)]
33. Hekinian, R.; Hoffert, M.; Larque, P.; Cheminee, J.L.; Stoffers, P.; Bideau, D. Hydrothermal Fe and Si oxyhydroxide deposits from South Pacific intraplate volcanoes and East Pacific rise axial and off-axial regions. *Econ. Geol.* **1993**, *88*, 2099–2121. [[CrossRef](#)]
34. Fallon, E.K.; Petersen, S.; Brooker, R.A.; Scott, T.B. Oxidative dissolution of hydrothermal mixed-sulphide ore: An assessment of current knowledge in relation to seafloor massive sulphide mining. *Ore Geol. Rev.* **2017**, *86*, 309–337. [[CrossRef](#)]

35. Kuksa, K.; Bich, A.; Cherkashov, G.; Firstova, A.; Kuznetsov, V.; Bel'tenev, V. Mass-wasting processes input in proximal metalliferous sediments: A case study of the Pobeda hydrothermal fields. *Mar. Geol.* **2021**, *438*, 106517. [[CrossRef](#)]
36. Hannington, M.; Herzig, P.; Scott, S.; Thompson, G.; Rona, P. Comparative mineralogy and geochemistry of gold-bearing sulfide deposits on the mid ocean ridges. *Mar. Geol.* **1991**, *101*, 217–248. [[CrossRef](#)]
37. Monecke, T.; Petersen, S.; Hannington, M.D.; Grant, H.; Samson, I.M. The minor element endowment of modern sea-floor massive sulfides and comparison with deposits hosted in ancient volcanic successions. *Econ. Geol.* **2016**, *18*, 245–306. [[CrossRef](#)]
38. Dubinin, A.V. *Rare Earth Element Geochemistry in the Ocean*; Nauka: Moscow, Russia, 2006; 360p. (In Russian)
39. Ayupova, N.R.; Maslennikov, V.V.; Kotlyarov, V.A.; Maslennikova, S.P.; Danyushevsky, L.V.; Large, R. Se and In minerals of in the submarine oxidation zone of the Molodezhnoe copper–zinc massive sulfide deposit. Southern Urals. *Dokl. Earth Sci.* **2017**, *473*, 318–322. [[CrossRef](#)]
40. Belogub, E.V.; Ayupova, N.R.; Krivovichev, V.G.; Novoselov, K.A.; Blinov, I.A.; Charykova, M.V. Se minerals in the continental and submarine oxidation zones of the South Urals volcanogenic-hosted massive sulfide deposits: A review. *Ore Geol. Rev.* **2020**, *122*, 103500. [[CrossRef](#)]
41. Benjamin, S.B.; Haymon, R.M. Hydrothermal mineral deposits and fossil biota from a young (0.1 Ma) abyssal hill on the flank of the fast spreading East Pacific rise: Evidence for pulsed hydrothermal flow and tectonic tapping of axial heat and fluids. *Geochem. Geophys. Geosyst.* **2006**, *7*, Q05002. [[CrossRef](#)]
42. Zeng, Z.; Wang, X.; Zhang, G.; Yin, X.; Chen, D.; Wang, X. Formation of Fe-oxyhydroxides from the East Pacific rise near latitude 13°N: Evidence from mineralogical and geochemical data. *Sci. China Ser. D Earth Sci.* **2008**, *51*, 206–215. [[CrossRef](#)]
43. Embile, R.F.; Walder, I.F.; Schuh, C.E.; Donatelli, J.L. Cu, Pb and Fe release from sulfide-containing tailings in seawater: Results from laboratory simulation of submarine tailings disposal. *Mar. Pollut. Bull.* **2018**, *137*, 582–592. [[CrossRef](#)] [[PubMed](#)]
44. Toner, B.M.; Rouxel, O.; Santelli, C.M.; Edwards, K.J. Sea-floor weathering of hydrothermal chimney sulfides at the East Pacific rise 9°N: Chemical speciation and isotopic signature of Iron using X-ray absorption spectroscopy and laser ablation MC-ICP-MS. *Geochim. Cosmochim. Acta Suppl.* **2008**, *72*, A951.
45. Beltenev, V.E.; Narkevsky, E.V.; Dobretsova, I.G.; Gablina, I.F.; Galkin, S.V.; Molodtsova, T.N.; Layba, A.A. The results of Professor Logatchev-37 cruise, MAR. In Proceedings of the XXI International Scientific Conference (school) on Marine Geology, Moscow, Russia, 16–20 November 2015; GEOS: Moscow, Russia, 2015; pp. 126–128. (In Russian).
46. Beltenev, V. *Polar Marine Geosurvey Expedition (PMGE) Report on Exploration Work on the Russian Exploration Area in Atlantic Ocean with an Estimate Forecast Resources of PMS of Categories P2–P3 in Blocks 31–45*; Unpublished Report; Polar Marine Geosurvey Expedition (PMGE): St. Petersburg, Russia, 2015; 266p. (In Russian)
47. Cherkashov, G.; Kuznetsov, V.; Kuksa, K.; Tabuns, E.; Maksimov, F.; Bel'tenev, V. Sulfide geochronology along the Northern Equatorial Mid-Atlantic Ridge. *Ore Geol. Rev.* **2017**, *87*, 147–154. [[CrossRef](#)]
48. Amplieva, E.E.; Bortnikov, N.S.; Kovalchuk, E.V.; Beltenev, V.E. The Pobeda modern submarine hydrothermal sulfide edifice cluster (Mid-Atlantic Ridge, 17 degrees 08'N): Mineralogy and chemical composition. In Proceedings of the 14th SGA Biennial Meeting, Mineral Resources to Discover, Quebec City, QC, Canada, 20–23 August 2017; 1–4, pp. 649–652.
49. Gablina, I.F.; Dobretsova, I.G.; Popova, E.A.; Dara, O.M.; Sadchikova, T.A.; Gor'kova, N.V.; Mikheev, V.V. Mineral composition and geochemical zoning of bottom sediments in the Pobeda hydrothermal cluster (17°07.45' N–17°08.7' N Mid-Atlantic Ridge). *Lithol. Miner. Resour.* **2021**, *56*, 113–131. [[CrossRef](#)]
50. Gablina, I.F.; Dobretsova, I.G.; Laiba, A.A.; Narkevsky, E.V.; Maksimov, F.E.; Kuznetsov, V.Y. Specific features of sulfide ores in the Pobeda hydrothermal cluster, Mid-Atlantic Rise 17°07'–17°08' N. *Lithol. Miner. Res.* **2018**, *53*, 431–454. [[CrossRef](#)]
51. Paton, C.; Hellstrom, J.; Paul, B.; Woodhead, J.; Hergt, J. Iolite: Freeware for the visualisation and processing of mass spectrometric data. *J. Anal. At. Spectrom.* **2011**, *26*, 2508–2518. [[CrossRef](#)]
52. Longerich, H.P.; Günther, D.; Jackson, S.E. Elemental fractionation in laser ablation inductively coupled plasma mass spectrometry. *Fresenius' J. Anal. Chem.* **1996**, *355*, 538–542. [[CrossRef](#)]
53. Large, R.R.; Danyushevsky, L.; Hollit, C.; Maslennikov, V.; Meffre, S.; Gilbert, S.; Bull, S.; Scott, R.; Emsbo, P.; Thomas, H.; et al. Gold and trace element zonation in pyrite using a laser imaging technique: Implications for the timing of gold in orogenic and Carlin-style sediment-hosted deposits. *Econ. Geol.* **2009**, *104*, 635–668. [[CrossRef](#)]
54. Large, R.R.; Maslennikov, V.V.; Robert, F.; Danyushevsky, L.V.; Chang, Z. Multistage sedimentary and metamorphic origin of pyrite and gold in the giant Sukhoi Log deposit, Lena gold province, Russia. *Econ. Geol.* **2007**, *102*, 1232–1267. [[CrossRef](#)]
55. Thomas, H.V.; Large, R.R.; Bull, S.W.; Maslennikov, V.V.; Berry, R.F.; Fraser, R.; Froud, S.; Moye, R. Pyrite and pyrrhotite textures and composition in sediments, laminated quartz veins, and reefs at Bendigo gold mine, Australia: Insights for ore genesis. *Econ. Geol.* **2011**, *106*, 1–31. [[CrossRef](#)]
56. Smirnov, V.I. *Correlation Methods in Paragenetic Analysis*; Nedra Publishers: Moscow, Russia, 1981; p. 174. (In Russian)
57. Hiram, M.V.; de Lima Toledo, F.A.; Junior, E.C.; Costa, K.B.; de Quadros, J.P. Q-Mode and R-Mode Factor Analysis in Quantitative Studies of Microfossils of the Late Quaternary in Sediments from the Brazilian Continental Margin. *Sci. Commun. Terræ* **2010**, *7*, 41–49.
58. Gablina, I.F.; Dobretsova, I.G.; Narkevskii, E.V.; Gustaitis, A.N.; Sadchikova, T.A.; Gor'kova, N.V.; Savichev, A.T.; Lyutkevich, A.D.; Dara, O.M. Influence of hydrothermal-metasomatic processes on the formation of present-day sulfide ores in carbonate bottom sediments of the mid-Atlantic Ridge (19°–20° N). *Lithol. Miner. Res.* **2017**, *52*, 335–357. [[CrossRef](#)]

59. Kuznetsov, V.Y.; Cherkashov, G.; Kuksa, K.; Firstova, A.; Maksimov, F.; Bel'tenev, V.; Lazareva, L.; Levchenko, S.; Baranova, N. Chronology of seafloor massive sulfides formation within the Pobeda hydrothermal cluster (MAR). *Geochronometria* **2020**, *47*, 63–70. [[CrossRef](#)]
60. Lyutkevich, A.D.; Gablina, I.F.; Dara, O.M.; Yapaskurt, V.O.; Shcherbakov, V.D.; Somov, P.A. Mineral Phases of Zinc in Ore-Bearing Sediments of the Pobeda Hydrothermal Cluster (17°07.45'–17°08.7' N MAR). *Lithol. Miner. Resour.* **2022**, *57*, 404–420. [[CrossRef](#)]
61. Zhabin, A.G.; Samsonova, N.S. Signs of disappeared pyrrhotite in VMS deposits. *Proc. Sov. Mineral. Soc.* **1975**, *103*, 346. (In Russian)
62. Grommet, L.P.; Dymek, R.F.; Haskin, L.A.; Korotev, R.L. The “North American shale composite”: Its composition, major and trace element characteristics. *Geochim. Cosmochim. Acta* **1984**, *48*, 2469–2482. [[CrossRef](#)]
63. Bruemmer, G.W.; Gerth, J.; Tiller, K.G. Reaction kinetics of the adsorption and desorption of nickel, zinc and cadmium by goethite. I. Adsorption and diffusion of metals. *Eur. J. Soil Sci.* **1988**, *39*, 37–52. [[CrossRef](#)]
64. Hrischeva, E.; Scott, S.D. Geochemistry and morphology of metalliferous sediments and oxyhydroxides from the Endeavour segment, Juan de Fuca Ridge. *Geochim. Cosmochim. Acta* **2007**, *71*, 3476–3497. [[CrossRef](#)]
65. Maslennikov, V.V.; Maslennikova, S.P.; Ayupova, N.R.; Zaykov, V.V.; Tseluyko, A.S.; Melekestseva, I.Y.; Large, R.R.; Danyushevsky, L.V.; Herrington, R.J.; Lein, A.T.; et al. Chimneys in Paleozoic massive sulfide mounds of the Urals VMS deposits: Mineral and trace element comparison with modern black, grey, white and clear smokers. *Ore Geol. Rev.* **2017**, *85*, 64–106. [[CrossRef](#)]
66. Edwards, K.J.; Mccollom, T.M.; Konishi, H.; Buseck, P.R. Seafloor bioalteration of sulfide minerals: Results from in situ incubation studies. *Geochim. Cosmochim. Acta* **2003**, *67*, 2843–2856. [[CrossRef](#)]
67. Janecky, D.R.; Shanks, W.C., III. Computational modeling of chemical and sulfur isotopic reaction processes in seafloor hydrothermal systems: Chimneys, massivesulfides, and subjacent alteration zones. *Can. Mineral.* **1988**, *26*, 805–825.
68. Woodruff, L.G.; Shanks, W.C., III. Sulfur isotope study of chimney minerals and vent fluids from 21°N, East Pacific Rise: Hydrothermal sulfur sources and disequilibrium sulfate reduction. *J. Geophys. Res.* **1988**, *93*, 4562–4572. [[CrossRef](#)]
69. Mozgova, N.N.; Borodaev, Y.S.; Gablina, I.F.; Cherkashev, G.A.; Stepanova, T.V. Mineral assemblages as indicators of the maturity of oceanic hydrothermal sulfide mounds. *Lithol. Min. Res.* **2005**, *40*, 293–319. [[CrossRef](#)]
70. Mozgova, N.N.; Efimov, A.V.; Borodaev, Y.S.; Krasnov, S.G.; Cherkashov, G.A.; Stepanova, T.V.; Ashadze, A.M. Mineralogy and chemistry of massive sulfides from the Logatchev hydrothermal field (14°45' N Mid-Atlantic Ridge). *Explor. Min. Geol.* **1999**, *8*, 379–395.
71. Keith, M.; Smith, D.J.; Jenkin, G.; Holwell, D.; Dye, M.D. A review of Te and Se systematics in hydrothermal pyrite from precious metal deposits: Insights into ore-forming processes. *Ore Geol. Rev.* **2017**, *96*, 269–282. [[CrossRef](#)]
72. Firstova, A.; Stapanova, T.; Sukhanova, A.; Cherkashov, G.; Poroshina, I. Au and Te minerals in seafloor massive sulphides from Semyenov-2 hydrothermal field, Mid-Atlantic ridge. *Minerals* **2019**, *9*, 294. [[CrossRef](#)]
73. Evrard, C.; Fouquet, Y.; Moelo, Y.; Rinnert, E.; Etoubleau, J.; Langlade, J.A. Tin concentration in hydrothermal sulfides related to ultramafic rocks along the Mid-Atlantic Ridge: A mineralogical study. *Eur. J. Mineral.* **2015**, *27*, 627–638. [[CrossRef](#)]
74. Melekestseva, I.Y.; Maslennikov, V.V.; Maslennikova, S.P.; Danyushevsky, L.; Large, R. Covellite from Semenov-2 hydrothermal field (13°31.13' N, Mid-Atlantic Ridge): Enrichment in trace elements according to LA-ICP-MS analysis. *Dokl. Earth Sci.* **2017**, *473*, 291–295. [[CrossRef](#)]
75. Fouquet, Y.; Walik, A.; Cambon, P.; Mevel, C.; Meyer, G.; Gente, P. Tectonic setting and mineralogical and geochemical zonation in the Snake Pit sulfide deposit (Mid-Atlantic Ridge at 23°N). *Econ. Geol.* **1993**, *88*, 2018–2036. [[CrossRef](#)]
76. Cook, N.J.; Ciobanu, C.L.; Pring, A.; Skinner, W.; Shimizu, M.; Danyushevsky, L.; Saini-Eidukat, B.; Melcher, F. Trace and minor elements in sphalerite: A LA-ICPMS study. *Geochim. Cosmochim. Acta* **2009**, *73*, 4761–4791. [[CrossRef](#)]
77. Von Damm, K.; Edmond, J.M.; Grant, B.; Measures, C. Chemistry of submarine hydrothermal solution at 21 N East Pacific Rise. *Geochim. Cosmochim. Acta* **1985**, *49*, 11347–11363. [[CrossRef](#)]
78. Lalou, C.; Brichet, E. Anomalously high uranium contents in the sediment under Galapagos hydrothermal mounds. *Nature* **1980**, *284*, 251–253. [[CrossRef](#)]
79. Emerson, S.R.; Husteded, S.S. Ocean anoxia and the concentrations of molybdenum and vanadium in seawater. *Mar. Chem.* **1991**, *34*, 177–196. [[CrossRef](#)]
80. Mikhaylichenko, A.I.; Mikhlin, E.B.; Patrikeev, Y.B. *Rare-Earth Metals; Metallurgy*: Moscow, Russia, 1987; p. 232. (In Russian)
81. Klopogge, J.T.; Ponce, C.P. Spectroscopic Studies of Synthetic and Natural Saponites: A Review. *Minerals* **2021**, *11*, 112. [[CrossRef](#)]
82. Martin, F.; Petit, S.; Decarreau, A.; Ildefonse, P.; Graubit, O.; Beziat, D.; de Parseval, P.; Noa, Y. Ga/Al substitutions in synthetic kaolinites and smectites. *Clay Miner.* **1998**, *33*, 231–241. [[CrossRef](#)]
83. Anantharamaiah, P.N.; Pattayil, J. Effect of size and site preference of trivalent non-magnetic metal ions (Al<sup>3+</sup>, Ga<sup>3+</sup>, In<sup>3+</sup>) substituted for Fe<sup>3+</sup> on the magnetostructural properties of sintered CoFe<sub>2</sub>O<sub>4</sub>. *J. Phys. D Appl. Phys.* **2017**, *50*, 435005. [[CrossRef](#)]
84. Gurvich, E.G. *Metalliferous Sediments of the World Ocean*; Springer: Berlin, Germany, 2006; 430p.
85. Cornel, R.M. Simultaneous incorporation of Mn, Ni and Co in the IOH (α-FeOOH) structure. *Clay Miner.* **1991**, *26*, 427–430. [[CrossRef](#)]
86. Moffett, J.W.; Ho, J. Oxidation of cobalt and manganese in sea water via a common microbially catalyzed pathway. *Geochim. Cosmochim. Acta* **1996**, *60*, 3415–3424. [[CrossRef](#)]

87. Martinez-Ruiz, F.; Paytan, A.M.; Gonzalez-Muñoz, T.; Jroundi, F.; Abad, M.M.; Lam, P.J.; Bishop, K.B.; Horner, T.J.; Morton, P.L.; Kastner, M. Barite formation in the ocean: Origin of amorphous and crystalline precipitates. *Chem. Geol.* **2019**, *511*, 441–451. [[CrossRef](#)]
88. Cao, Y.; Guo, Q.; Shu, Z.; Jiao, C.; Luo, L.; Guo, W.; Zhao, Q.; Yin, Z. Tungstate removal from aqueous solution by nanocrystalline iowaite: An iron-bearing layered double hydroxide. *Environ. Pollut.* **2019**, *247*, 118–127. [[CrossRef](#)]
89. Bogdanov, Y.A.; Lisizin, A.P.; Sagalevich, A.M.; Gurchich, E.G. *Hydrothermal Ore Genesis on Ocean Floor*; Nauka: Moscow, Russia, 2006; 527p. (In Russian)
90. Shanks, W.S. Stable isotope in seafloor hydrothermal systems: Vent fluids, hydrothermal deposits, hydrothermal alteration, and microbial processes. *Rev. Mineral. Geochem.* **2001**, *43*, 469–526. [[CrossRef](#)]
91. Bolanz, R.M.; Wierzbicka-Wieczorek, M.; Čaplovičová, M.; Uhlík, P.; Göttlicher, J. Structural Incorporation of As<sup>5+</sup> into Hematite. *Environ. Sci. Technol.* **2013**, *47*, 9140–9147. [[CrossRef](#)] [[PubMed](#)]
92. Feely, R.A.; Trefry, J.H.; Massoth, G.J.; Metz, S. A comparison of the scavenging of phosphate and arsenic from seawater by hydrothermal iron oxyhydroxides in the Atlantic and Pacific Ocean. *Deep-Sea Res.* **1991**, *38*, 617–623. [[CrossRef](#)]
93. Rudnicki, M.; Elderfield, H. A chemical model of the buoyant and neutrally buoyant plume above the TAG vent field, 26°N, Mid-Atlantic Ridge. *Geochim. Cosmochim. Acta* **1993**, *57*, 2939–2957. [[CrossRef](#)]
94. German, C.R.; Colley, S.; Palmer, M.R.; Khripounoff, A.; Klinkhammer, G.P. Hydrothermal plume-particle fluxes at 13°N on the East Pacific Rise. *Deep. Sea Res. Part I Oceanogr. Res. Pap.* **2002**, *49*, 1921–1940. [[CrossRef](#)]
95. Dubinin, A.V. Geochemistry of iron-calcium hydroxophosphates in pelagic sediments: Origin and compositional evolution in the course of diagenesis. *Geochem. Intern.* **2001**, *39*, 585–596.
96. Melghit, K.; Al-Mungi, A.S. New form of iron orthovanadate FeVO<sub>4</sub>·1.5H<sub>2</sub>O prepared at normal pressure and low temperature. *Mater. Sci. Eng.* **2007**, *136*, 177–181. [[CrossRef](#)]
97. Elderfield, H.; Whitfield, M.; Burton, J.D.; Bacon, M.P.; Liss, P.S. The oceanic chemistry of the rare-earth elements. *Philos. Trans. R. Soc. Lond.* **1988**, *A325*, 105–126.
98. Zhang, L.; Tao, C.; Su, X.; Lv, S.; Zhou, J.; Deng, X.; Yu, C.; Song, B. Characteristics of rare earth elements in the surface sediments of Southwest Indian Ridge: Implication of grain size for the identification of hydrothermal activity. *Geo-Mar. Lett.* **2022**, *42*, 7. [[CrossRef](#)]
99. Boynton, W.V. Geochemistry of Rare Earth Elements: Meteorite Studies. In *Rare Earth Element Geochemistry*; Henderson, P., Ed.; Elsevier: New York, NY, USA, 1984; pp. 63–114. [[CrossRef](#)]
100. Bruland, K.W.; Lohan, M.C. Controls of trace elements in sea water. In *The Ocean and Marine Geochemistry*; Holland, H.D., Turekian, K.K., Eds.; Elsevier: Amsterdam, The Netherlands, 2004; pp. 23–47.
101. Sverjevsky, D.A. Europium redox equilibria in aqueous solution. *Eart Planet. Sci. Lett.* **1984**, *67*, 70–78. [[CrossRef](#)]
102. Bao, S.; Zhou, H.; Peng, X.; Ji, F.; Yao, H. Geochemistry of REE and yttrium in hydrothermal fluids from Endeavor segment, Juan de Fuca Ridge. *Geochem. J.* **2008**, *42*, 359–370. [[CrossRef](#)]
103. Bau, M. Rare earth element mobility during hydrothermal and metamorphic fluid-rock interaction and the significance of the oxidation state on Eu. *Chem. Geol.* **1991**, *93*, 219–230. [[CrossRef](#)]
104. Maslennikov, V.V.; Maslennikova, S.P.; Lein, A.Y. *Mineralogy and Geochemistry of Ancient and Modern Black Smokers*; Russian Academy of Science: Moscow, Russia, 2019; 832p. (In Russian)

**Disclaimer/Publisher’s Note:** The statements, opinions and data contained in all publications are solely those of the individual author(s) and contributor(s) and not of MDPI and/or the editor(s). MDPI and/or the editor(s) disclaim responsibility for any injury to people or property resulting from any ideas, methods, instructions or products referred to in the content.